Multi-instrument remote and *in situ* observations of the Erebus Volcano (Antarctica) lava lake in 2005: A comparison with the Pele lava lake on the jovian moon Io

Ashley Gerard Davies [a,*], Julie Calkins [b,1], Lucas Scharenbroich [a], R. Greg Vaughan [a], Robert Wright [c], Philip Kyle [b], Rebecca Castaño [a], Steve Chien [a], Daniel Tran [a]

[a] Jet Propulsion Laboratory-California Institute of Technology, 4800 Oak Grove Drive, Pasadena, CA 91109-8099, United States
[b] Department of Earth & Environmental Science, New Mexico Institute of Mining and Technology, 801 Leroy Place, Socorro, NM 87801, United States
[c] Hawai'i Institute of Geophysics and Planetology, University of Hawai'i at Manoa, 1680 East-West Road, Honolulu, HI, 96822, United States

ARTICLE INFO

ABSTRACT

The stable, persistent, active lava lake at Erebus volcano (Ross Island, Antarctica) provides an excellent thermal target for analysis of spacecraft observations, and for testing new technology. In the austral summer of 2005 visible and infrared observations of the Erebus lava lake were obtained with sensors on three space vehicles *Terra* (ASTER, MODIS), *Aqua* (MODIS) and *EO-1* (Hyperion, ALI). Contemporaneous ground-based observations were obtained with hand-held infrared cameras. This allowed a quantitative comparison of the thermal data obtained from different instruments, and of the analytical techniques used to analyze the data, both with and without the constraints imposed by ground-truth. From the thermal camera data, in December 2005 the main Erebus lava lake (Ray Lake) had an area of ≈ 820 m^2. Surface colour temperatures ranged from 575 K to 1090 K, with a broad peak in the distribution from 730 K to 850 K. Total heat loss was estimated at 23.5 MW. The flux density was ≈ 29 kW m^{-2}. Mass flux was estimated at 64 to 93 kg s^{-1}. The best correlation between thermal emission and emitting area was obtained with ASTER, which has the best combination of spatial resolution and wavelength coverage, especially in the thermal infrared. The high surface temperature of the lava lake means that Hyperion data are for the most part saturated. Uncertainties, introduced by the need to remove incident sunlight cause the thermal emission from the Hyperion data to be a factor of about two greater than that measured by hand-held thermal camera. MODIS also over-estimated thermal output from the lava lake by the same factor of two because it was detecting reflected sunlight from the rest of the pixel area. The measurement of the detailed temperature distribution on the surface of an active terrestrial lava lake will allow testing of thermal emission models used to interpret remote-sensing data of volcanism on Io, where no such ground-truth exists. Although the Erebus lava lake is four orders of magnitude smaller than the lava lake at Pele on Io, the shape of the integrated thermal emission spectra are similar. Thermal emission from this style of effusive volcanism appears to be invariant. Excess thermal emission in most Pele spectra (compared to Erebus) at short wavelengths (<3 μm) is most likely due to disruption of the surface on the lava lake by escaping volatiles.

1. Introduction

Active lava lakes are found at the top of an open magma system and provide insight into the magma supply and circulation process in volcanic conduits. Persistent lava lakes are rare volcanic phenomena on Earth and the best known examples are currently found at Erta'Ale volcano, Ethiopia; Nyiragongo volcano, Democratic Republic of Congo; and Erebus volcano, Ross Island, Antarctica (Fig. 1). Erebus is the world's southernmost active volcano and is the focus of this study. Active silicate (>1000 K)

volcanism also occurs elsewhere in the Solar System. The jovian satellite Io is the most volcanically active body in the Solar System and has some features that exhibit the temporal, thermal and spectral characteristics of lava lakes (see a summary of Io's volcanism in Davies, 2007).

Eruption of basalt lavas is the most common form of silicate volcanism on Earth, with an eruption temperature of ≈ 1150 °C (1423 K). Io's volcanoes, discovered in 1979 by the NASA *Voyager* spacecraft (Morabito et al., 1979), were originally thought to be dominated by sulphur volcanism at temperatures not exceeding ≈ 700 K. Ground-based telescope observations in the 1980s and 1990s (e.g., Johnson et al., 1988; Veeder et al., 1994; Blaney et al., 1995; Stansberry et al., 1997) revealed the presence of thermal sources at temperatures in excess of 1000 K, indicative of silicate volcanism.

The National Aeronautics and Space Administration (NASA) *Galileo* spacecraft carried out multiple flybys of Io between 1995 and 2003. It

---
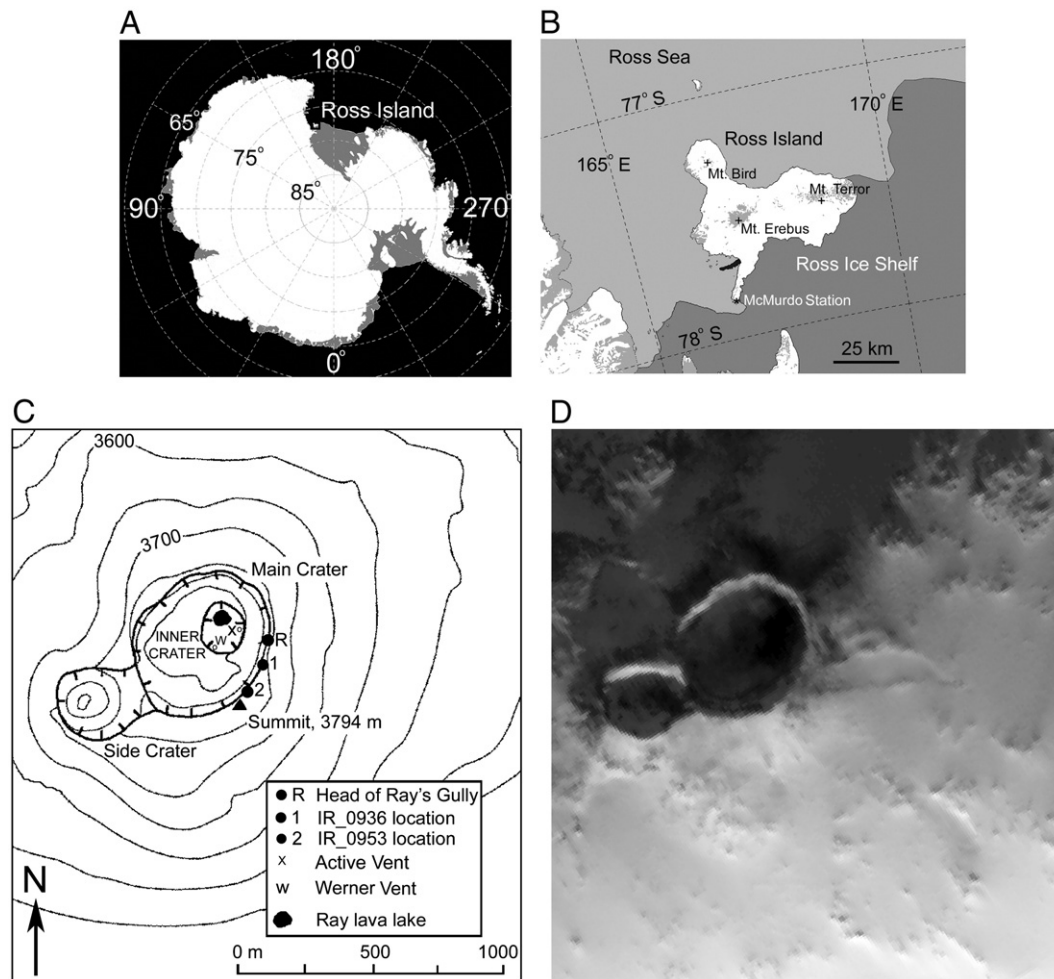
Fig. 1. Location and features. (A) Antarctica, with the position of Ross Island indicated. (B) Ross Island and environs. (C) Sketch map of the summit crater of Mt. Erebus, Antarctica, based the map shown in Harris et al. (1999a) and references therein. The locations on the rim of the main crater from where thermal camera observations were made of the lava lake (Ray Lake) are indicated. The Werner Vent and Active Vent were not visible from any of these locations. (D) The summit area as seen by *EO-1* ALI, at 10 m pixel^{-1} (observation EO1A2005347130520_PF1_01_PAN [PAN band]).

made observations at visible wavelengths with the Solid State Imaging experiment (SSI) (Belton et al., 1992) and in the short-wavelength infrared (SWIR) with the Near Infrared Mapping Spectrometer (NIMS) (Carlson et al., 1992). These data allowed the identification of multiple hot spots. Many had components in excess of 1000 K, indicative of silicate volcanism (Davies et al., 1997; McEwen et al., 1997, 1998a,b; Davies et al., 2001; Keszthelyi et al., 2001; Davies, 2003a). A list of all high-temperature (>1000 K) hot spots is given in Davies (2007).

Magma eruption temperatures in excess of 1800 K, indicative of ultramafic volcanism, were derived from *Galileo* data at Pillan (McEwen et al., 1998b; Davies et al., 2001), the site of a massive eruption in 1997. However, these temperatures were difficult to resolve with models of Io's interior structure (Keszthelyi et al., 2004) and a reappraisal of the methodology used to interpret the data determined that ultramafic-composition lavas were not required to explain the *Galileo* SSI data (Keszthelyi et al., 2007).

Analysis of the *Galileo* dataset highlights the difficulty of determining magma eruption temperature from remote-sensing data. On Earth the composition of the magma is usually known or well-constrained. For example, Hawaiian basalt erupts at a temperature of ≈1430 K and the eruption temperature of the anorthoclase phonolite lava at Erebus is ≈1273 K (Calkins et al., 2008-this issue). Such knowledge of eruption temperature and the lava's cooling behavior can be used to constrain the analysis of terrestrial remote-sensing data. On Io, not even the composition of the erupting magma is known. Instead, it has to be inferred from derived temperatures.

Most data of Io's volcanoes are at resolutions of hundreds of kilometers per pixel and, apart from a handful of spacecraft observations, the volcanic thermal source is sub-pixel. Multi-wavelength and hyperspectral data yield the integrated thermal emission spectrum of the eruption, the sum of thermal emission from all emitting surfaces. To interpret these data, models of volcanic thermal emission have been developed (Carr, 1986; Davies, 1996; Howell, 1997, 2006; Davies et al., 2001, 2005). These models generate the expected thermal emission from different styles of eruption (e.g., insulated lava flow, lava lake, and lava fountain, alone and in combination) and have been applied with success to Io data. For example, between 1996 and 2000 the *Galileo* spacecraft obtained a number of low-resolution observations of the Ionian volcano Pele with NIMS. Thermal emission from Pele consistently peaks at around 3 μm, a wavelength that indicates a very hot average surface temperature (≈1030 K). A surface at this temperature is newly exposed (i.e., erupted) and cools rapidly. Yet in data collected over more than two decades there is no evidence of a shift in the peak of thermal emission to longer wavelengths that would indicate the presence of cooling or cooled lava flows at Pele. Analysis of the *Galileo* Pele data with a volcanic thermal emission model (Davies, 1996) led Davies et al. (2001) to conclude that the most likely explanation was that Pele was an active, overturning lava lake. This hypothesis was greatly supported by high-resolution images later obtained by SSI (Radebaugh et al., 2004).

Questions remain, however. How accurate are the models of thermal emission that have been applied to Io? How robust are the

results? This paper describes the first steps in determining the accuracy of the models, and, indeed, the whole approach that has generated a considerable body of work over the last 20 years. We acquired spacecraft and ground-based infrared data of volcanic activity at an active lava lake. We detail how these data are processed to determine the temperature and area distribution, and how the data are used to create the integrated thermal emission spectrum. It is against this product that the volcanic thermal emission model of Davies (1996) can be tested. The results of these tests are presented elsewhere (Davies et al., 2008).

2. Erebus volcano, Antarctica

The most persistent lava lake, named Ray Lake, at Erebus volcano is situated on the floor of the volcano's Inner Crater (see Fig. 1). It was first observed in the early 1970s (Giggenbach et al., 1973) and has been present active ever since (Kyle et al., 1982, Kyle, 1994; Aster et al., 2004). The volcano is only accessible during the short austral summer. Satellite remote sensing provides year-round monitoring of thermal flux from the volcano (Wright, and Pilger, 2008-this issue). These data can now be compared with *in situ* data of volcanic activity from sensors installed on the volcano (Aster et al., 2004). Harris et al. (1999a) reviewed the remote sensing of Erebus using the *Landsat* Thematic Mapper (TM) and Advanced Very High Resolution Radio-meter (AVHRR). They demonstrated the value of satellite remote sensing by estimating thermal and mass fluxes from observations of Erebus. These satellite data allowed a rough estimate of the area of the lava lake, found to be ≈2800 m^2 prior to September 1984. The lake was briefly buried in late 1984 but re-established itself in January 1985 with an area of 180–630 m^2. Estimates of effusion rate ranged from 330±167 kg s^{-1} prior to 1984 to 30–76 kg s^{-1} thereafter, indicating a reduction in magma supply to the lava lake, and an according reduction in activity, during 1984 (Harris et al., 1999b).

Additionally, a strong case was made for monitoring Erebus to determine the contribution of aerosols and gases from the volcano to the Antarctic atmosphere to assess the impact on the environment and delicate ecosystem (Zreda-Gostynska et al., 1997; Wardell et al., 2003, 2004).

Recently the inauguration of a new generation of instruments on polar orbiting satellites has provided new tools for thermal observations. These include the Hyperion hyperspectral imager (Pearlman et al., 2003) and Advanced Land Imager (ALI) multi-spectral imager (Ungar et al., 2003) on the *Earth Observing 1* (*EO-1*) spacecraft (launched in 2000); the Advanced Spaceborne Thermal Emission and Reflectance Radiometer (ASTER) (Yamaguchi et al., 1998) on *Terra* (launched in 1999); and the Moderate Resolution Imaging Spectro-meter (MODIS) (Salomonson et al., 1989) on *Terra* and *Aqua* (the latter launched in 2002). These instruments have made thousands of observations of volcanoes all over the world. We report here on the spacecraft and ground observations made of the Erebus lava lake in late 2005.

Erebus volcano (77.53° S, 167.17° W) is a particularly attractive target for study. The high latitude of Erebus allows for more frequent observations from spacecraft in highly-inclined polar orbits as adjacent ground tracks for polar orbiters converge towards the poles. These spacecraft include *Terra*, *Aqua*, and *EO-1*, the operations of which are described below. Erebus is a relatively stable, constantly active thermal source, and is therefore highly suitable for testing new instruments and technology (for example: the Autonomous Science-craft Experiment, described below); and finally, there is an extensive network of sensors on the volcano operated by the Mount Erebus Volcano Observatory at the New Mexico Institute of Mining and Technology (monitoring seismic activity, tilt, gas emission and detecting and measuring the acoustic signatures of frequent Strom-bolian eruptions (e.g., Aster et al., 2004; Johnson et al., 2008-this issue; Jones et al., 2008-this issue).

3. Observations and the field campaign 2005

During the short austral summer of 2005, visible and infrared observations of the Erebus lava lake were obtained with visible and infrared sensors on *Terra*, *Aqua* and *EO-1* (Figs. 1 and 2). The *EO-1* observations were part of an ongoing program of global monitoring of dynamic processes being carried out by NASA's New Millennium Program Autonomous Sciencecraft Experiment (ASE) (Chien et al., 2005; Davies et al., 2006a; Doggett et al., 2006; Ip et al., 2006). ASE is software that autonomously processes and analyzes Hyperion hyperspectral data (described below) onboard *EO-1*, with identifica-tion of dynamic events driving subsequent spacecraft operations. With the spacecraft incorporated into an autonomous sensor web, run from NASA's Jet Propulsion Laboratory in Pasadena, CA, alerts from other spacecraft and ground-based sensors are used to trigger spacecraft observations (Chien et al., 2005; Davies et al., 2006b). The observation campaign, which began in early 2004, had obtained 137 observations of Erebus by December 2006.
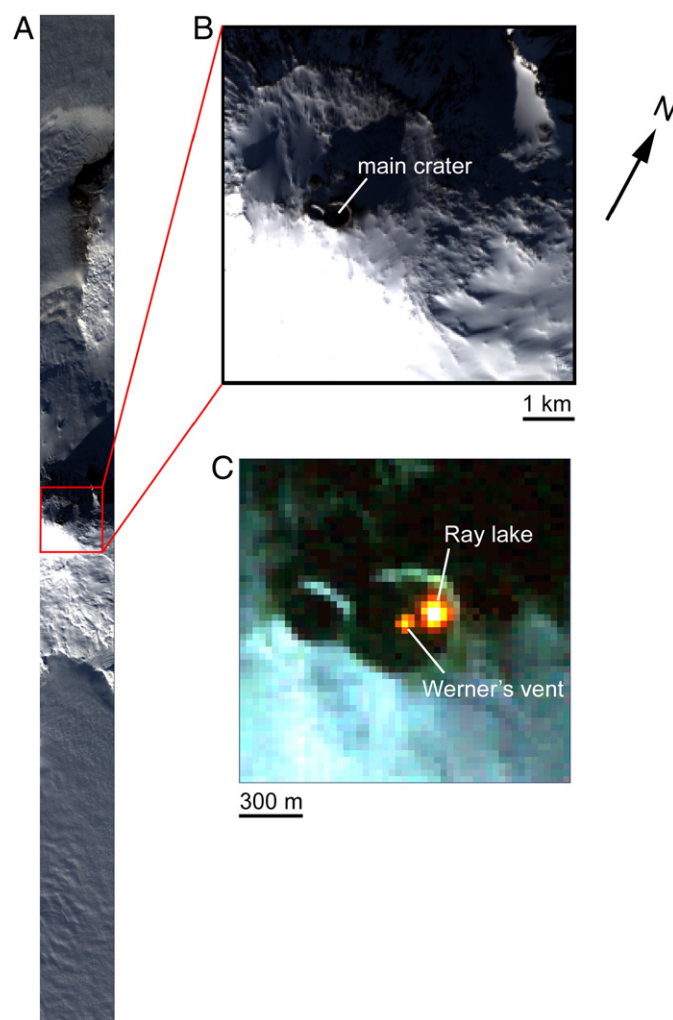

Fig. 2. Hyperion observes of Erebus volcano. Hyperion on *EO-1* observed Erebus volcano on 2005 December 13 at 13:05:22 UT (observation identifier EO1H2221282005347110KF). (A) The full Hyperion observation swath (256×3460 pixels, or 7.7 km×103.8 km) is at a resolution of 30 m pixel^{-1}. Data are obtained at 220 wavelengths from 0.4 to 2.5 μm. The image is made from three bands at 0.630 μm (band 28), 0.549 μm (band 20) and 0.478 μm (band 13). (B) Detail of the summit area showing the main crater, at the bottom of which lies the active lava lake (Ray Lake). (C) Ray Lake and the nearby Werner Vent (see Fig. 1) show up clearly at short infrared wavelengths. Thermal blooming and detector cross talk, the result of detector saturation, make these thermal anomalies appear larger than they actually are. This image was created from data at 2.285 μm (band 213), 1.649 μm (band 150) and 1.245 μm (band 110).

Some of these observations were validated with hand-held infrared cameras, in order to provide ground-truth for satellite data analysis, allowing quantitative comparison of techniques used to analyse each dataset. The analyses have been carried out both in the absence of the ground-truth data, and constrained by ground-truth data.
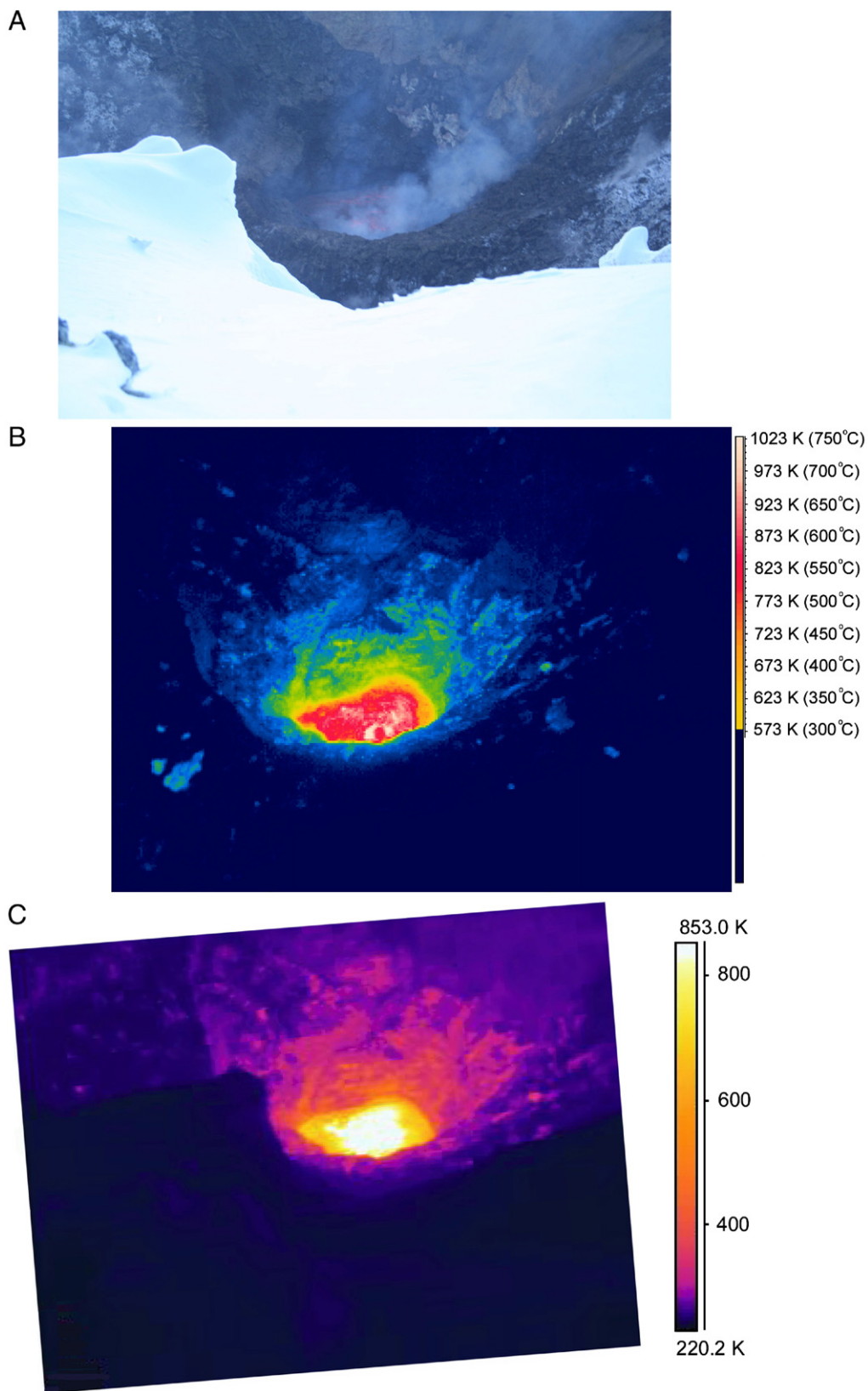
Fig. 3. Ground-truth data obtained contemporaneously with the Hyperion observation EO1H2221282005347110KF shown in Fig. 2. (A) Visible wavelength image (Canon Digital Rebel). (B) FLIR ThermaCAM P65 image (image identifier IR_0936). None of the pixels in the lake are outside of the camera sensitivity range (550 K to 1800 K). Temperatures peak in excess of 1000 K. (C) FLIR ThermaCAM EX320 image. Much of the EX320 data are saturated (>773 K). The slant distance to target is 380 m.

Contemporaneous spacecraft observations are therefore also collected in daylight, with a reflected sunlight component that has to be corrected for in SWIR data. The sunlight component is somewhat mitigated by the location of the lava lake itself, which was, at the time of the ground-truthed spacecraft observations, always in deep shadow.

Over many years of *in situ* observations, three thermal sources have been identified on the floor of the Erebus summit crater (Calkins et al., 2008-this issue) (Fig. 1). The first feature is Ray Lake, the persistent lava lake that is the most persistent and largest thermal feature. The second feature is the Active Vent, which has infrequent eruptions mainly of ash and, rarely, lava bombs, and is a much smaller feature (aerially and thermally) than Ray Lake. The third high-profile thermal source is a small vent called Werner Vent which is usually incandescent but periodically fills with magma and forms a transient lava lake (Werner lava lake). Werner Vent (or lake) is located ~60 m southwest of Ray Lake. Werner lava lake was not present in late 2005, but was ≈1000 m^2 in surface area in late 2004 (Calkins et al., 2008-this issue). The Werner Vent or Lake can be often identified as a separate thermal feature to Ray Lake in spacecraft data.

Ray Lake is confined by a prominent rim that is built up of phonolite spatter and lava bombs erupted from the lake. The lava in the lake forms a rough, rubbly crust, very different from the relatively smooth crust that forms on Hawaiian basalt lava lakes. The lake surface crust is heavily cracked, revealing hotter, reddish magma beneath. Occasionally, on a scale of a few minutes, small areas of the crust bulge and rupture, releasing puffs of gas. In December 2005, although the lava lake appeared to be static, time lapse photography showed that lava was welling up from the centre of the lake, spreading laterally and descending at the lake margins.

Larger Strombolian eruptions were taking place every 6 to 9 h. There was little hint beforehand that such an event was about to take place: the lava lake surface would start to bulge slightly and then, only a second or two later, would violently explode (Aster et al., 2004). The explosions ejected lava bombs, some over 2 m in diameter, out of the crater to distances in excess of 1 km. After the explosion, the evacuated lake would rapidly fill with lava from the conduit and, within a few minutes, there was no indication from the appearance of the lake that the explosion had ever occurred.

Ray Lake (Figs. 1 and 2) is located at the bottom of the Inner Crater which lies at the north end of the Main Crater floor. The best viewing position in December 2005 was obtained from locations on the crater rim close to the summit (at 3794 m [Fig. 1]). From the rim of the crater, the distance to the centre of the lava lake, as measured by laser rangefinder, was 380 or 412 m, depending on which of the two observation sites were chosen.

4. Hand-held infrared imagers and area of the lava lake

4.1. Instrument description

The development of hand-held, highly-sensitive, calibrated thermal imagers that are capable of obtaining unsaturated images of high-temperature surfaces has revolutionised field volcanology, yielding data at high spatial resolutions across a wide temperature range (e.g., Wright and Flynn, 2003). Such observations capture the full distribution of temperature across active lava bodies. We used FLIR Systems Inc. infrared cameras ThermaCAM P65 and a ThermaCAM EX320 to obtain images of Ray Lake that were contemporaneous with spacecraft observations.

The ThermaCAM P65 used in 2005 had an upper temperature detection limit of 1773 K (1500 °C). Because the magma liquidus temperature does not exceed ≈1300 K this setting was suitable to obtain unsaturated data from the hottest areas of the lava lake. The lower temperature limit for this range was 573 K. The EX320 model had a temperature range of 273 K to 773 K and was used to measure temperatures below the temperature detection limit of the P65. The P65 data were at or above its lower temperature detection limit.

Image size for both cameras was 320×240 pixels, with a field of view of 24°×18°. Sequences of images were obtained 10 s apart, bracketing the brief period of time when spacecraft passed overhead and collected data. The best FLIR data and best observing conditions for spacecraft (no clouds at or above the summit of the volcano, and almost no plume emanating from the lava lake) were obtained on 2005 December 13, 13:05:26 UT for an *EO-1* pass, and again at 2005 December 13, 14:00:19 UT, for a *Terra* pass.

Examples of images obtained with the two FLIR imagers and a visible-wavelength digital camera are shown in Fig. 3. These images were obtained as close as possible (within ±5 s) to the Hyperion and ALI observations (Fig. 2) obtained at 2005 December 13, 13:05:26 UT.

The following settings were used for the thermal cameras: emissivity=0.96, reflected temperature=293.1 K, atmospheric temperature=243.0 K, and relative humidity=20%. For image IR_0936, the distance to target (380 m) and the P65 instrument field of view (24°×18°, 320 pixels by 240 pixels) yield an apparent pixel size of 0.248 m^2. With a viewing angle, from vertical, of 57°, applying a cosine correction yields a pixel area of 0.455 m^2. The area was used to determine heat loss from the lava lake, effusion rate, and flux density.

4.2. Temperature and area distribution from ground-based data

Fig. 4 shows the temperatures on the surface of the lava lake, ranging from 575 K to 1090 K. There is a broad peak in the distribution from ≈730 to ≈850 K. The temperature with the highest frequency is 765 K. The flat distribution of temperatures from 860 K to 1030 K is due to (1) cracks in the crust on the surface of the lake, (2) areas where the crust is disrupted revealing hotter lava beneath, and (3) very young surfaces where upwelling magma reaches the surface and spreads laterally. Each pixel is treated as isothermal, but because the area covered by a pixel is 0.455 m^2, each pixel probably contains different areas at different temperatures. A small high-temperature crack fraction within each pixel may be present. The thermal camera determines the averaged temperature from the measured radiation from all areas at all detectable temperatures within the pixel. The total heat loss from the surface of the lava lake Q_{tot} (W) is given by

$$Q_{tot} = Q_{rad} + Q_{conv} \qquad (1)$$

where Q_{rad} (W) is heat lost by radiation and Q_{conv} (W) is heat lost via atmospheric convection. Atmospheric convection is either forced (Q_{force}) in the presence of wind, or natural (Q_{nat}), whichever term is the greater.

The integrated thermal emission from the lava lake Q_{rad} is found by summing the thermal emission from each pixel (from $x = 1$ to N,
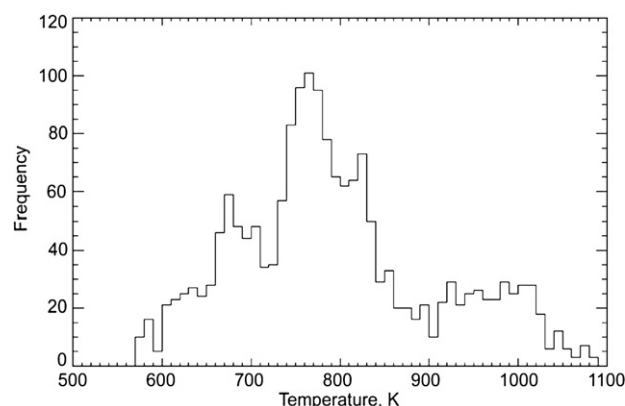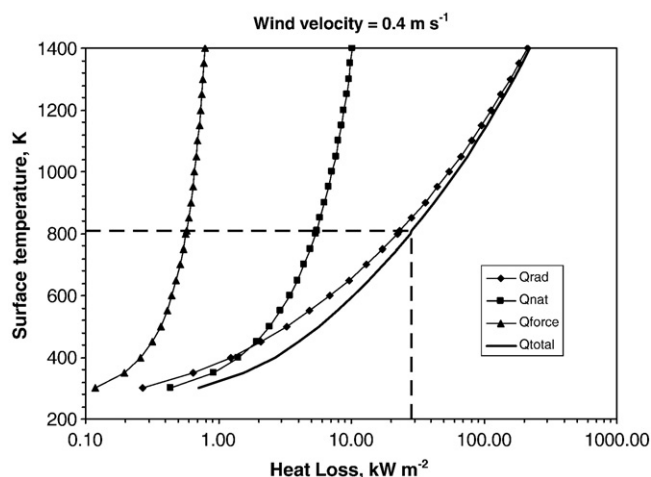

Fig. 4. Distribution in number of pixels of colour temperatures on surface of Ray Lake (ThermaCAM P65 observation IR_0936). The bin size is 10 K. A broad peak in the distribution is seen between ≈730 K and ≈850 K. The most frequent temperature is 765 K. The integrated thermal emission profile is generated from these data.

Fig. 5. Calculation of heat loss from the surface of Ray Lake as a function of surface temperature. In the absence of wind (so forced convection [Q_{force}]=0 W m^{-2}) total heat loss is the sum of heat loss by radiation (Q_{rad}) and natural convection (Q_{nat}) in the terrestrial atmosphere, as derived using the methodology of Head and Wilson (1986). The heavy dashed line shows the values of Q_{nat} (5.5 kW m^{-2}) and Q_{force} (23.2 kW m^{-2}) at the effective lava lake surface temperature T_{eff} of 807 K. Total heat loss at this temperature is 28.6 MW. The wind velocity in this case is 0.4 m s^{-1}.

Table 1

a. Ray Lake (lava lake) eruption parameters: Mount Erebus, December 2005

	Units		
IR Camera observation ID		IR_0936	IR_0953
Date (UT), time	yymmmdd	05DEC13	05DEC13
	hh:mm:ss	13:05:26	14:00:19
Area of lake	m^2	820	817
Radiative heat loss Q_{rad}	MW	19.80	18.90
Convective heat loss Q_{conv}	MW	4.48	4.47
Total heat loss Q_{tot}	MW	24.28	23.37
Mass flux	kg s^{-1}	67–93	64–89
Flux density	kW m^{-2} s^{-1}	29.6	28.6
Mass density	kg m^{-2} s^{-1}	0.08–0.11	0.08–0.11

b. Lava lake eruption parameters: Pele, Io

	Units		
Galileo NIMS Observation		G8INVOLCAN02	16INHRSPEC01
Date	yymmmdd	97MAY7	98JUL20
Area of lake	m^2	3.1×10^7	1.6×10^7
Radiative heat loss	MW	2.0×10^5	2.4×10^5
Convective heat loss	MW	–	–
Total heat loss	MW	2.0×10^5	2.4×10^5
Mass flux	kg s^{-1}	537,000–741,000	644,000–889,000
Flux density	kW m^{-2} s^{-1}	6	17
Mass density	kg m^{-2} s^{-1}	0.02–0.023	0.04–0.05

Davies et al. (2001).

where N is the number of pixels covering the lake) of the lava lake, such that

$$Q_{rad} = \sum_{x=1}^{x=N} \left(T_{pix}^4 - T_{env}^4\right) \varepsilon \, \sigma \, A_{pix} \qquad (2)$$

where T_{pix}^4 is the pixel temperature, T_{env}^4 is the environment temperature (233 K), ε is the lava emissivity (0.96), σ is the Stefan–Boltzmann constant (5.67×10^{-8} W m^{-2} K^{-4}), and A_{pix} is the pixel area. For ThermaCAM P65 image IR_0936, A_{pix}=0.455 m^2. Eq. (2) yields Q_{rad} = 19.8 MW.

Q_{force}, forced convective heat loss per unit surface area of the lava lake, is given by

$$Q_{force} = W f(T_{surf} - T_{env})\rho_{atmos} c_{p,atmos} \qquad (3)$$

where W is wind speed (m s^{-1}), f is a friction factor equal to 0.0036 (Greeley and Iverson, 1987; Keszthelyi and Denlinger, 1996), T_{surf} is the

temperature of the lava surface, T_{env} is the temperature of the atmosphere, ρ_{atmos} is the atmospheric density and $c_{p,atmos}$ is the atmosphere specific heat capacity at constant pressure. ρ_{atmos} and $c_{p,atmos}$ are evaluated at the mean temperature of the silicate-atmosphere interface $(T_{surf}+T_{env})/2$.

In accounting for heat loss via convection, the possibilities of natural and forced convection (e.g. with an 'external' forcing agent, such as wind) need be to considered. Weather conditions on the summit of Erebus on 2005 December 13 were ideal, with no wind, and no clouds above the summit. Additionally, there was relatively little visible plume from the lava lake. The convective heat loss mechanism from the lake was therefore taken to be natural, not forced. Head and Wilson (1986) showed that heat loss due to natural convection (Q_{nat}) is given by

$$Q_{nat} = A \left(\frac{c_{p,atmos} \, \rho_{atmos}^2 \, g \, \beta (T_{surf} - T_{env})}{\eta_{atmos} \, k_{atmos}}\right)^{1/3} (T_{surf} - T_{env}) k_{atmos} \qquad (4)$$

where k_{atmos} is the thermal conductivity of the atmosphere, η_{atmos} is the viscosity of the atmosphere; g is the acceleration due to gravity,
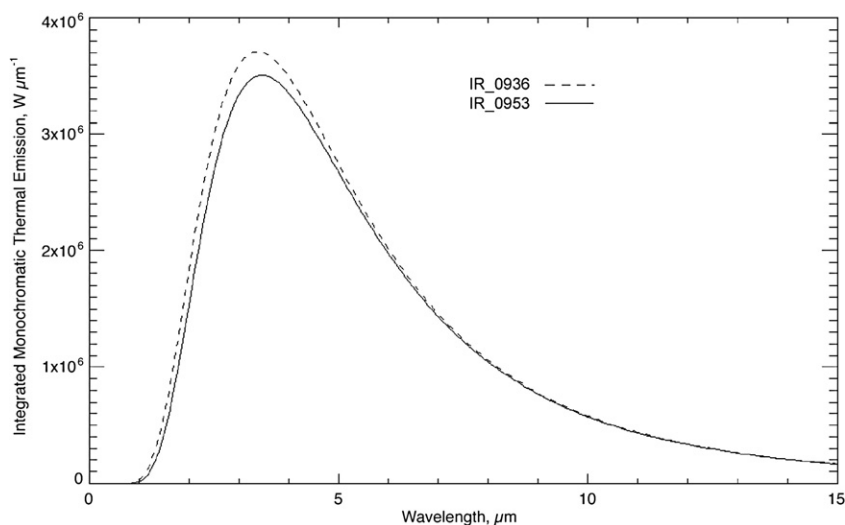
Fig. 6. Integrated thermal emission spectra from the Erebus lava lake (Ray Lake), as determined from FLIR data. The dotted line is derived from image IR_0936 obtained simultaneously with a Hyperion image, and the solid line is derived from image IR_0953, obtained simultaneously with an ASTER image. There is little variation over the 55 min between observations. The peak of the thermal emission at 3.4 μm is consistent with the thermal emission spectrum of an active, overturning lava lake (Davies, 2007).

β is the volume expansion coefficient of air; and A is a dimensionless factor reflecting the physical geometry of the system. For a heated plate facing upwards and for turbulent air movement, $A = 0.14$ (McAdams, 1954).

The average surface temperature of the lava lake, T_{eff} (K), the temperature that yields the observed value of Q_{rad}, from area A_{lake}, is found by rearranging Eq. (2), such that

$$T_{eff} = \sqrt[4]{\frac{Q_{rad}}{\varepsilon \sigma A_{lake}} + T_{env}^4}. \tag{5}$$

From Eq. (5), $T_{eff} = 807$ K. The natural convection term is derived from Head and Wilson (1986) who calculated atmospheric natural convection (Q_{nat}) as a function of surface temperature (Fig. 5). Alternatively, evaluating Eq. (4) for T_{eff}, $Q_{nat} = 4.6 \times 10^3$ W m^{-2}, or 4.55×10^6 W from the entire lake. From Eq. (1), adding Q_{rad} and Q_{nat} yields $Q_{tot} = 23.5$ MW.

4.3. Integrated thermal emission spectrum: the basis for comparison

The lava lake integrated thermal emission spectrum is created by summing the thermal emission from each pixel such that the monochromatic thermal emission $Q_{(\lambda, T_N)}$ in W μm^{-1} at wavelength λ (μm) is given by

$$Q_{(\lambda, T_N)} = \sum_{x=1}^{x=N} \frac{c_1 A_{pix}}{\lambda^5 (e^{c_2 / \lambda T_N} - 1)} \varepsilon \tag{6}$$

where N is the number of pixels covering the lake, T_N is the temperature of pixel N (K), A_{pix} = is the area of each pixel, ε = emissivity (0.96), $c_1 = 3.7413 \times 10^8$ W μm^4 m^{-2} and $c_2 = 1.4388 \times 10^4$ μm K. The integrated thermal emission spectra for the ThermaCAM P65 observations contemporaneous with the Hyperion (IR_0936) and ASTER (IR_0953) observations on 2005 December 13 is shown in Fig. 6. In both cases, the peak of thermal emission is at 3.4 μm, close to that expected for T_{surf} of 807 K. It is to this spectrum that model-derived estimates of temperature and area distribution and total thermal emission from remote-sensing assets can be compared. We take this as the established ground-truth.

4.4. Mass flux and mass density estimates

For the basis of comparison with other analyses, we use the equation for mass flux used by Harris et al. (1999a), where heat loss from the lava lake is balanced by heat yielded from magma circulating through the system. Magma rises up to the surface, partially solidifies, and then sinks. Mass flux M (kg s^{-1}) is given by

$$M = \frac{Q_{rad} + Q_{conv}}{C_L \Delta f + C_{magma} \Delta T_{magma}} \tag{7}$$

where C_L is the latent heat of crystallization, Δf is the crystallised mass fraction, C_{magma} is the specific heat capacity of the magma, and ΔT_{magma} is the amount of cooling of the magma from liquidus to lake temperature. Using $C_L = 3 \times 10^5$ J kg^{-1}, $\Delta f = 0.3$ to 0.45, $C_{magma} = 1150$ J kg^{-1} K^{-1}, and $\Delta T_{magma} = 150$ K to 200 K, the mass flux M is in the range 64 kg s^{-1} to 93 kg s^{-1}. These numbers can be compared with other estimates of mass flux at Erebus. Harris et al. (1999a) derived mass fluxes of 330 ± 167 kg s^{-1} prior to 1984 to 30–76 kg s^{-1} after 1984. In November and December 2004, when there were two lava lakes present (Calkins et al., 2008-this issue), the mass flux needed to sustain the total observed radiated heat output of 54–61 MW (34–37 MW from Ray Lake and 20–24 MW from Werner Lake) was ≈270–710 kg s^{-1} (Calkins et al., 2008-this issue).

Two useful metrics for comparing the vigor of different eruptions and different styles of lava emplacement are flux density (the thermal emission per unit area) and mass density (the mass erupted per unit area of active surface). The more vigorous the eruption, the more incandescent material is exposed, and the higher the flux density tends to be (Davies and Keszthelyi, 2005). Flux and mass densities for Erebus, as well as other eruption parameters, are shown in Table 1a. The flux density values of ≈29 kW m^{-2} are almost identical to those obtained for both Ray (25.8 kW m^{-2}) and Werner (23.3–28.0 kW m^{-2}) lakes in 2004 (Calkins et al., 2008-this issue). Although one of the lakes had disappeared in 2005, the manner in which lava was circulating through the system, losing heat at the surface, appeared to be unchanged.

5. EO-1 and Terra observations

We now describe the spacecraft observations obtained at the same time as the FLIR observations of the lava lake. Data were obtained by Hyperion, ALI, ASTER and MODIS, on EOS satellites Terra and Aqua and on EO-1. Details of these observations are shown in Table 2. Instrument characteristics are shown in Table 3. These multispectral and hyperspectral imagers represent significant improvements from previous imagers such as Landsat ETM, in terms of spatial, spectral and temporal resolutions obtained. Terra, Aqua, and EO-1 are in high-inclination polar orbits at an altitude of approximately 705 km, with orbital periods of 98.9 min. These orbits yield multiple observation opportunities of targets at high latitudes. Erebus, located at ≈77 °S, is therefore a prime target. The different space-based instruments span a wide range of spatial and spectral resolutions across a wavelength range encompassing the visible to the thermal infrared.

EO-1 was the first in NASA's New Millennium Program Earth Observation series. EO-1 was launched in November 2000 into a circular orbit with an inclination of 98.2°. The velocity of the EO-1 nadir point is 6.74 km s^{-1}. Its orbit yields global coverage, with exact ground-repeat tracks every 16 days. EO-1 is a pointable spacecraft.

For equatorial targets, observations can be nadir, or up to two paths to the east or west. This pointing angle translates to more than 6 paths east or west at latitudes above 70°, greatly increasing the frequency of observations. Given the topography of the Erebus summit crater and the location of the lava lake in a pit in the bottom of the crater, observations were limited to those less than 29° from vertical in order to image the entire lava lake (see Harris et al., 1999a).

5.1. Hyperion and ALI observations

5.1.1. Instrument descriptions

The Hyperion imaging spectrometer on EO-1 is a hyperspectral instrument, that is, one capable of more than 100 measurements of radiance in a single spectrum. High spectral resolution (10 nm) is achieved. Hyperion, with 220 discrete usable bands covering a wavelength range of 0.4 to 2.5 μm, is currently the only instrument of this kind in Earth orbit. The spectral range makes Hyperion an ideal instrument for detecting the heat from the hottest areas (>500 K) of ongoing volcanic activity (Davies et al., 2006a).

The spatial resolution $R_{spatial}$ of a spacecraft sensor is given by

$$R_{spatial} = S\Omega \tag{8}$$

where S is range to target and Ω is the instrument field of view. Hyperion has $\Omega = 4.3 \times 10^{-5}$ radians. Range S of a nadir observation is 7.05×10^5 m (705 km). From Eq. (9), $R_{spatial}$ is 30 m. The area of a pixel A_{pix} is therefore

$$A_{pix} = (S\Omega)^2 \tag{9}$$

or 900 m^2 for Hyperion.

Table 2
Selection of spacecraft and FLIR observations of Erebus in December 2005

Instrument	Day of year	Date (UTC)	Time (UTC)	Hyperion observation ID	Hyperion pass or ASTER orbit	FLIR observations	FLIR location	Comments
Hyperion/ALI	341	7-Dec-05	13:53:06	EO1H2221282005341110KF	EAST4		–	
Hyperion/ALI	341	7-Dec-05	20:22:xx	EO1H0551152005341110KF	WEST		–	
Hyperion/ALI	342	8-Dec-05	12:56:14	EO1H2221282005342110KF	EAST6		–	
Hyperion/ALI	343	9-Dec-05	13:37:12	EO1H2221282005343110KF	WEST	JC,KJ,AG	UEH	Recon. Lake not fully visible
ASTER/MODIS	343	9-Dec-05	14:24:54		31795	JC,KJ,AG	UEH	Recon. Lake not fully visible
Hyperion/ALI	343	9-Dec-05	20:07:04	E01H0551152005343110KF	EAST2	AGD,EM,ND	UEH+	Recon. Lake not fully visible
ASTER/MODIS	343	9-Dec-05	20:55:14		31799	AGD,EM,ND	UEH+	Recon. Lake not fully visible
Hyperion/ALI	345	11-Dec-05	13:21:18	EO1H2221282005345110KF	EAST2	AGD,ND,EM	R	Problems with FLIR
ASTER/MODIS	345	11-Dec-05	14:12:54		31824	AGD,ND,EM	R	Problems with FLIR
Hyperion/ALI	345	11-Dec-05	19:51:10	EO1H0551152005345110KF	EAST4	JC,KJ,AG	R	Some plume. Good data
ASTER/MODIS	345	11-Dec-05	20:43:10		31828	JC,KJ,AG	R	Some plume. Good data
Hyperion/ALI	346	12-Dec-05	14:02:13	EO1H2221282005346110KF	WEST5		–	
Hyperion/ALI	346	12-Dec-05	20:32:07	EO1H0551152005346110KF	WEST3		–	
Hyperion/ALI	347	13-Dec-05	13:05:26	EO1H2221282005347110KF	EAST5	AGD,JC,AG	1, a	Little plume. Best data
ASTER/MODIS	347	13-Dec-05	14:00:19		31853	AGD,JC,AG	2, b	Little plume. Best data
ASTER/MODIS	347	13-Dec-05	20:30:39		31857		–	
Hyperion/ALI	348	14-Dec-05	13:46:03	EO1H2221282005348110KF	WEST2		–	
Hyperion/ALI	348	14-Dec-05	20:15:50	EO1H0551152005348110KF	NADIR		–	
ASTER/MODIS	349	15-Dec-05	13:48:09		31882		–	Backup (not needed)
ASTER/MODIS	349	15-Dec-05	20:18:29		31886		–	Backup (not needed)
Hyperion/ALI	350	16-Dec-05	13:29:34	EO1H2221282005350110KF	EAST		–	
Hyperion/ALI	350	16-Dec-05	19:59:20	EO1H0551152005350110KF	EAST3		–	
Hyperion/ALI	351	17-Dec-05	20:39:59	EO1H0551152005351110KF	WEST4		–	
Hyperion/ALI	351	17-Dec-05	14:10	EO1H0551152005350110KF	WEST6		–	
Hyperion/ALI	352	18-Dec-05	19:42	EO1H2221282005352110KF	EAST3		–	

Key

Hyperion/ALI	*EO-1* day observation
ASTER/MODIS	ASTER observation
Hyperion/ALI	*EO-1* Night observation
ASTER/MODIS	Backup observation in event of cloud etc.
352	On *EO-1* observation calendar
352	On *Terra* observation calendar
352	Contingency observations
352	Not selected
2:21:18	Groundtruthed observation
14:02:13	Observation obtained, no groundtruth

Notes.

a   FLIR image IR_0936
b   FLIR image IR_0953

AG=Alexander Gerst; AGD = Ashley Davies: EM = Elizabeth Morton; JC = Julie Calkins; KJ = Kyle Jones; ND = Nelia Dunbar

UEH = rim above Upper Erebus Hut on west side of summit. The crater was full of plume, but the FLIR unit could identify the lava lake location. There was not a clear view into the lake, although part of the surface could be seen.

UEH+ = high point about Upper Erebus Hut, south of UEH point. No view of the entire lava lake surface.

R = Crater rim at the head of Ray's Gully. This affords a clear view of Ray Lake (see Figure 1).
1 = Main crater rim location 1 (see Figure 1). Clear view of Ray Lake.
2 = Main crater rim location 2 (see Figure 1). Clear view of Ray Lake.

Table 3
Spacecraft instrument capabilities[a]

Spacecraft	EO-1	EO-1	Terra[b]	Terra
Instrument	Hyperion	ALI	ASTER	MODIS
Bands: range	220:	PAN: VIS	1–3: VIS–NIR	1–2: VIS
	VIS–SWIR	1–9: VIS–SWIR	4–9: SWIR	3–7: SWIR
			10–14: TIR	8–36: SWIR–TIR
Wavelength	0.4–2.5	0.4–0.69 (PAN)	0.52–0.86 (1–3)	0.62–0.67 (1–2)
coverage, μm	(1–220)	0.4–2.5 (1–9)	1.60–2.43 (4–9)	0.46–2.16 (3–7)
(bands)			8.125–11.65	0.41–14.4 (8–36)
			(10–14)	
Resolution,	30	10 (PAN)	15 (1–3)	250 (1–2)
m/pixel (bands)		30 (1–9)	30 (4–9)	500 (3–7)
			90 (10–14)	1000 (8–36)
Observations	14	14	7	22+
obtained				
7–18 Dec. 2005				

VIS = visible.
NIR = near infrared.
SWIR = short wavelength infrared.
TIR = thermal infrared.
  [a] 1999 EOS Reference Handbook http://eos.nasa.gov.
  [b] See Table 5 for more details.

The power output P_λ (W μm^{-1}) from a pixel as a function of wavelength is derived from the measured radiance I_λ (W m^{-2} str^{-1} μm^{-1}), which for terrestrial data has been corrected for atmospheric absorption. Power output is given by

$$P_\lambda = I_\lambda \pi (S\Omega)^2 / \cos\theta \qquad (10)$$

where θ is the emission angle in degrees.

The spectrum shape can be fitted with a blackbody curve or a combination of blackbody curves. Once a colour temperature T_c (K) has been determined, the thermal output per unit area $Q_{(\lambda, T_c)}$ (W m^{-2} μm^{-1}) can be calculated. The area A of the sub-pixel thermal source is therefore the total energy detected at wavelength λ (P_λ) divided by $Q_{(\lambda, T_c)}$, such that

$$A = P_\lambda / Q_{(\lambda, T_c)}. \qquad (11)$$

A Hyperion observation swath is 7.7 km (256 pixels) wide and extended collects can be up to 185 km long. The processing of Hyperion data and the extraction of colour temperature are described in Davies et al. (2006a).

ALI, the Advanced Land Imager, is a multispectral instrument with 10 bands covering 0.4 to 2.4 μm. The PAN (panchromatic) band covers 0.48–0.69 μm at a resolution of 10 m pixel^{-1}. The other 9 bands cover the visible and near-infrared to the SWIR with data at a spatial resolution of 30 m pixel^{-1}, the same as that obtained by Hyperion. The PAN band is not sensitive to temperatures encountered during volcanic activity. ALI data are collected in four swaths covering an area 37 km wide and 42 to 185 km in length. Fig. 1 shows a detail of one swath from ALI observation EO1A2005347130520_PF1_01_PAN (PAN band) and EO1A2005347130520_PF1_01 (ALI band 7, covering 1.2 to 1.3 μm). These data were obtained at the same time as the Hyperion data on 2005 December 13 UT.

Some caveats must be noted when using Hyperion to observe active volcanism. Firstly, the pixels may saturate, rendering data at wavelengths greater than ≈1.6 μm (see Supplemental Material and Fig. 7) unusable for the purposes of quantifying thermal emission (see Davies et al., 2006a). However, unsaturated data at shorter wavelengths can be used. Unfortunately, these are the wavelengths that are most strongly affected by sunlight. Although nighttime observations are best for studying short-wavelength volcanic thermal emission, it is not possible to obtain concurrent ground-truth during the Antarctic winter.

Additionally, an intense thermal source generates an "echo", always 11 samples to the left and one line down if the swath is displayed with the direction of travel towards the bottom of the page. This is most likely caused by electronic cross-talk (see text and Fig. 8 in Davies et al., 2006a) and is often seen in Erebus data. The 30 m pixel^{-1} scale places these anomalous pixels outside the summit crater, allowing easy identification of them.

5.1.2. EO-1 observations of Erebus, December 2005

Spacecraft observations of Erebus obtained with contemporaneous in situ thermal camera data are shown in Table 2. Of particular importance are the observations obtained on 2005 December 13 UT under excellent viewing conditions.

Visible and infrared Hyperion images are shown in Fig. 3. Fig. 3C is a detail of the observation at infrared wavelengths and shows the location of Ray Lake (the main lava lake) and the Active Vent. It should be noted that no thermal camera data were obtained of the ash vent. This is clearly a separate thermal source in the Hyperion data. Being much smaller and cooler than the lava lake, the ash vent contributes a small fraction of the total thermal emission observed. Both Ray Lake and the Werner Vent appear within a single MODIS pixel. Both features appear as separate thermal sources in ASTER TIR data.

The size of the thermal source in the Hyperion infrared data at wavelengths of approximately 2 μm is considerably larger than the size of the thermal source on the ground, which has an area (817 m^2) slightly less than the area of a single Hyperion pixel (900 m^2). Coincident with the location of the lava lake, the spectra of a 2×2 block of pixels in the Hyperion data show saturation at wavelengths beyond 1.6 μm (Fig. 7).

Each of these pixels probably contains some of the lava lake area. The "thermal echo" effect generates ghost pixels eleven pixels over and one line down. Additionally, the intense pixels are surrounded by other less intense pixels that are visible in the infrared data and that are readily detected by the ASE Thermal classifier running on EO-1 (see Davies et al., 2006a). It is not readily apparent what is causing these "hot" pixels. There is no surface heating outside of the lava lake that can be detected by the FLIR cameras. The atmosphere in the crater surrounding the lava lake is, similarly, not hot enough in FLIR images to be detected by Hyperion at SWIR wavelengths. The most likely explanation is that of another manifestation of detector cross-talk causing a "blooming" of the thermal signal.

This is an important discovery. Estimating the area of thermal sources in Hyperion data should be carried out with care because this blooming effect, coupled with the "thermal echo" can lead to over-estimation of the emitting area. The thermal echo is less of a problem as it always appears in the same place relative to pixels saturated at long Hyperion wavelengths.

5.1.3. Deriving temperature and area in Hyperion data: the Scharenbroich algorithm

In order to determine thermal emission from Hyperion data and calculate the temperature, area and thermal emission distributions, the Hyperion data has to be corrected for atmospheric absorption and the reflected solar component removed from the daytime data. The method we use is described in detail in the Supplemental Material. Figs. 8 and 9 show, respectively, the colour temperatures of the sub-pixel thermal sources and the fraction of the pixel each occupies. For the four pixels that display saturation, the resulting temperatures and areas are shown in Table 4. The total area of the lava lake is estimated to be 909 m^2. The total thermal emission (using Eq. (2)) is MW. This is slightly more than double the thermal emission measured with the hand-held infrared camera. Nevertheless, this is a favorable result given that most of the Hyperion spectral data were saturated and therefore not usable, and that the remaining data were those most affected by incident sunlight, which had to be removed. Other pixels in the crater showed thermal sources with high temperatures, but very small areas. These detections are from (1) the fitting of noise in the data, and (2) detector cross-talk. Better results would be obtained

from nighttime data, where uncertainties introduced by sunlight removal are not present.

5.2. Aster observations

5.2.1. Instrumentation and data

The ASTER instrument, mounted on the *Terra* spacecraft, measures radiance in 14 spectral channels in the visible, near infrared, short wave infrared (VIS, NIR, SWIR), and the thermal infrared (TIR) wavelength region (Yamaguchi et al., 1998). The VIS/NIR, SWIR and TIR radiance data are measured by three different subsystems, each with its own telescope, detector array and different spatial resolution (Table 3).

ASTER data were acquired of Mount Erebus at 14:00:21 UT on 2005 December 13 (Fig. 10). All 14 channels were acquired with the normal radiometric gain settings (i.e., not with "volcano mode" settings [see Wright et al., 1999]). Atmospherically corrected radiance data were used to measure surface radiance variations and calculate the thermal characteristics of the lava lake. For the ASTER surface radiance data products (AST09XT for the VIS–NIR/SWIR channels; AST09T for the TIR channels), the atmospheric correction methods and correction for the cross-talk effect in the SWIR channels are described in Thome et al.

(1998) and Tonooka and Iwasaki (2003), and the atmospheric correction methods for the TIR data are described in Gillespie et al. (1998). ASTER level 1B at-sensor radiance data were also used for SWIR data analysis. In addition, ASTER surface kinetic temperature data (AST08) and surface emissivity data (AST05) were derived using the temperature-emissivity separation (TεS) method of Gillespie et al. (1998), and were used to determine the thermal characteristics of the area surrounding the lava lake. These data were also compared to pixel-integrated temperatures that were derived from the radiance data.

5.2.2. Observing volcanic thermal activity with aster

The calculation of temperatures from remotely measured radiance is based on the Planck equation. Atmospherically corrected surface radiance as a function of wavelength (L_λ) can be rewritten from Eq. (6) as such:

$$L_\lambda = \frac{\varepsilon_\lambda c_1}{\lambda^5 (e^{c_2/\lambda T} - 1)} \qquad (12)$$

where, ε_λ = spectral emissivity, and T = temperature. Because thermal volcanic features are often smaller in spatial extent than the area covered by larger pixels, the radiance measured is a pixel-integrated
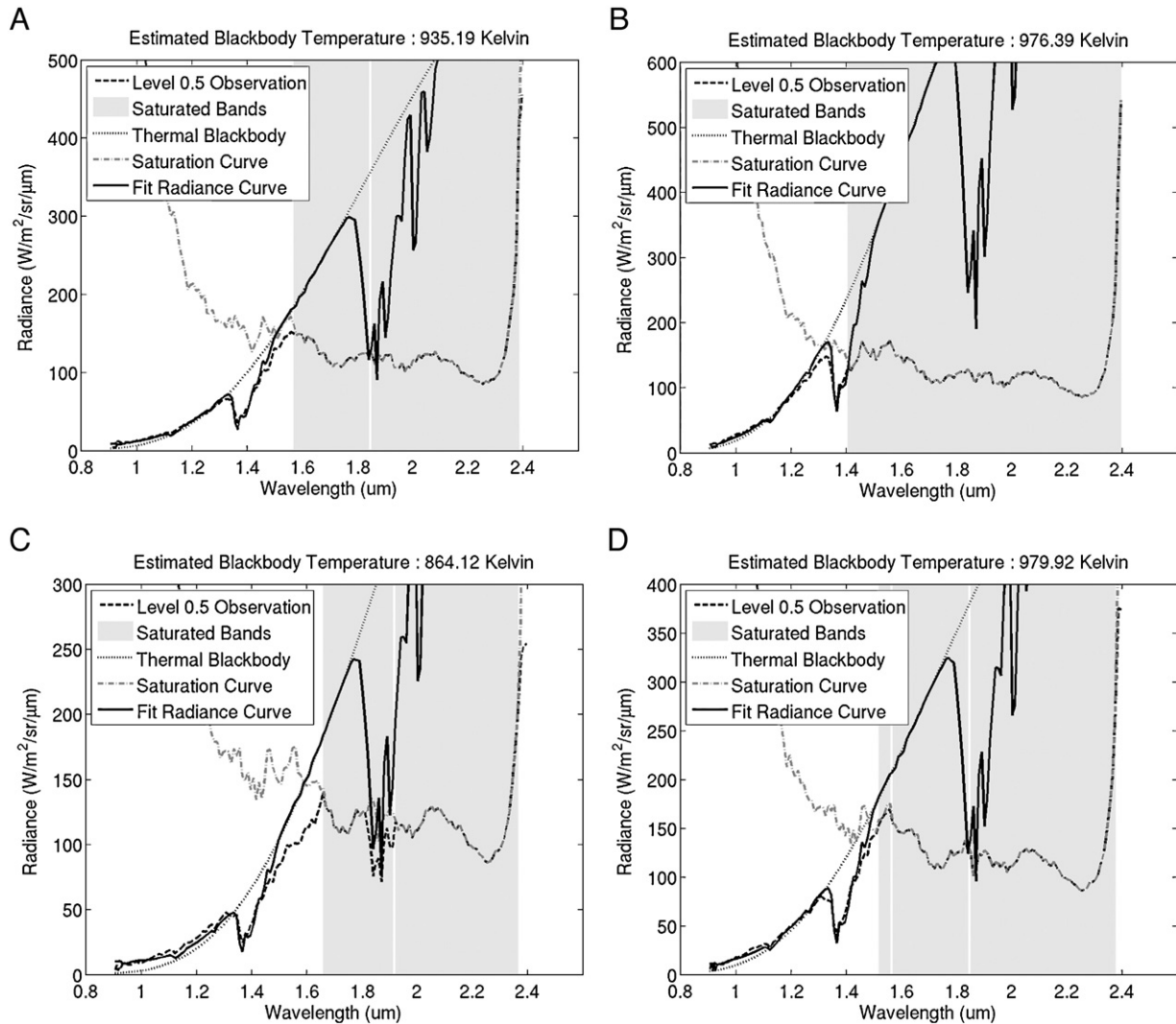
Fig. 7. Spectra and analysis of the four pixels in Hyperion observation EO1H222128200347110KF that cover the lava lake, showing the fitted radiance curve to the observed radiance values (black line). The methodology for doing this is described in the Supplemental Material. The gray areas cover the wavelengths that are affected by detector saturation, and which therefore provide only weak information on the lava lake temperature. The dotted line is the saturation point for each Hyperion detector. A = sample 160, line 1720. B = 181, line 1720. C = sample 180, line 1721. D = 181, line 1721. Derived temperatures and areas are shown in Figs. 8 and 9, and Table 4.
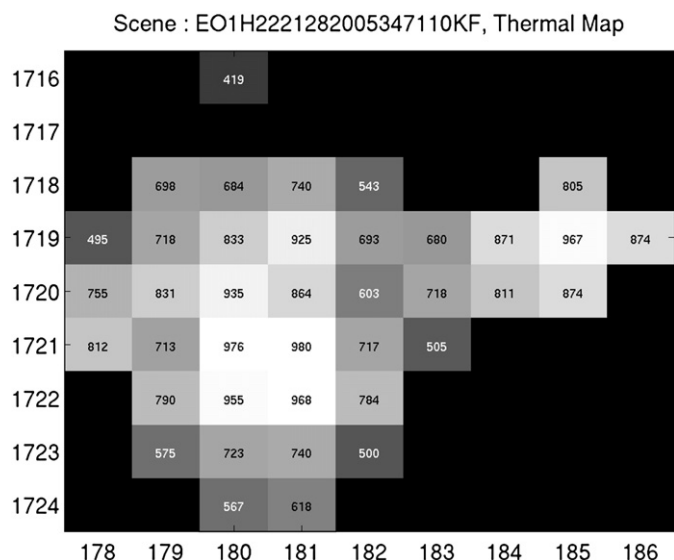
Fig. 8. Colour temperature of sub-pixel thermal anomalies derived from using the Scharenbroich data processing methodology (see Supplemental Material). Hyperion observation ID is EO1H222128200347110KF. Spectra of the 4 pixels covering the lava lake are shown in Fig. 7. Estimates of thermal emission are given in Table 4.

radiance that is an area-weighted sum of multiple sub-pixel radiating components. A temperature derived from the radiance data, whether by inversion of the Planck function or by temperature-emissivity separation, is therefore a pixel-integrated temperature (PIT). Pixel-integrated temperatures were calculated from the surface radiance data for a given wavelength by assuming an emissivity and solving the Planck equation for temperature (T).

Spectral emissivities for solid surfaces within the volcanic crater were derived from laboratory spectral measurements of basanite (sample # mewy_237bs) from the ASTER spectral library (http://speclib.jpl.nasa.gov). Although the Erebus lava is phonolitic in composition, basanite is a similar, slightly more Ca-rich volcanic rock, and would be spectrally very similar to phonolite, for which there are no known laboratory spectral measurements. The spectral
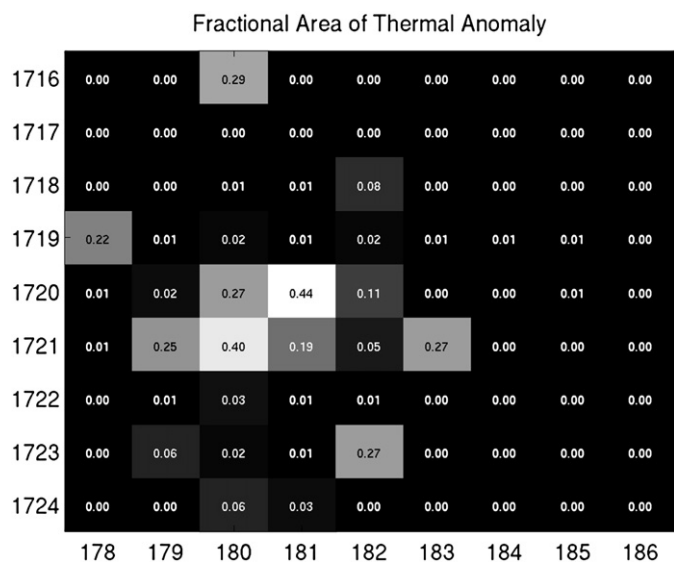
Fig. 9. Fractional pixel areas of thermal sources at the temperatures shown in Fig. 8. Hyperion observation ID is EO1H222128200347110KF. From source area and temperature the total thermal emission can be quantified (Table 4).

Table 4
Lava lake pixels in Hyperion observation EO1H2221282005347110KF L0.5 data: results from application of the Scharenbroich algorithm (Appendix A)

Swath column (L1 data)[a]	Swath line (L1 data)[a]	Pixel area fraction[b]	Area (m²)	Temperature (K)	Thermal emission[c] (MW)
180	1720	0.27	243	935	10.1
181	1720	0.23	207	907	7.6
180	1721	0.32	288	995	15.3
181	1721	0.19	171	983	8.7
Total[d]			909		41.7

[a] See Figs. 8 and 9.
[b] Pixel area is 900 m².
[c] Using emissivity of 0.96.
[d] Total thermal emission as determined from the FLIR data is 18.9 MW.

emissivities of basanite resampled to the spectral response functions of the ASTER channels are shown in Table 5. Theoretically, spectral emissivities for molten or nearly molten lava should be different than for solid lavas. Abtahi et al. (2002) reported field-measured TIR broadband emissivities for molten basaltic lavas as low as 0.5. No such measurements have been made at Ray Lake. However, ASTER surface emissivity data derived using the TεS method indicate relatively low spectral emissivities for the two pixels that contain the lava lake. While these values are almost certainly pixel-integrated emissivities from different sub-pixel components, they are more similar to the expected emissivity values for a molten lava component based on Abtahi et al. (2002), and thus more suitable emissivity assumptions for the hottest temperature component in the sub-pixel thermal models discussed below.

A method for calculating the fractional area and temperature sub-pixel thermal components using concurrent multispectral measurements was first described by Dozier (1981) and has since been developed and used in many studies of volcanic thermal sources (Rothery et al., 1988; Pieri et al., 1990; Harris et al., 1999a,b; Pieri and Abrams, 2005; Harris and Ripepe, 2007). A lava lake surface is typically composed of multiple temperature components, but for sufficiently small pixels can be simplified into two components, a hot molten core, and a cooler semi-solid crust (Harris et al., 1999a). The pixel-integrated radiance (R_λ) emitted at wavelength λ, and corrected for atmospheric affects, can be written as

$$R_\lambda = \varepsilon_\lambda \left[p_h L_{\lambda(T_h)} + p_c L_{\lambda(T_c)} \right] \qquad (13)$$

where p_c=portion of the pixel occupied by crusted (cooled) lava; p_h= portion of the pixel occupied by hot lava; L_λ=Planck radiance from a blackbody at temperature T and wavelength λ (see Eq. (12)) and T_c and T_h are the temperatures of the crust and hot molten lava, respectively.

Larger pixels can be modelled with three temperature components, the molten lava core and cooler semi-solid crust on the lava lake surface, and a third non-lava lake background component (discussed in the TIR section below).

5.2.3. VIS–NIR data analysis (15-m pixels)

At the time of ASTER data acquisition, ground-based measurements indicated that the lava lake was ≈32 m in diameter (area≈ 820 m²). For the 15-m VIS–NIR pixels, this means that the radiance measured for up to 9 pixels could have been influenced by lava lake thermal emission and between 1 and 4 pixels were likely dominated by lava lake thermal emission. Surfaces not associated with the lava lake or other thermal features in the crater that are at temperatures lower than ≈900 K (627 °C) do not radiate measurably in this wavelength range; therefore any radiance measured for non-thermal areas in the crater was assumed to be solar reflected radiance. An average solar reflected radiance was measured for each VIS–NIR
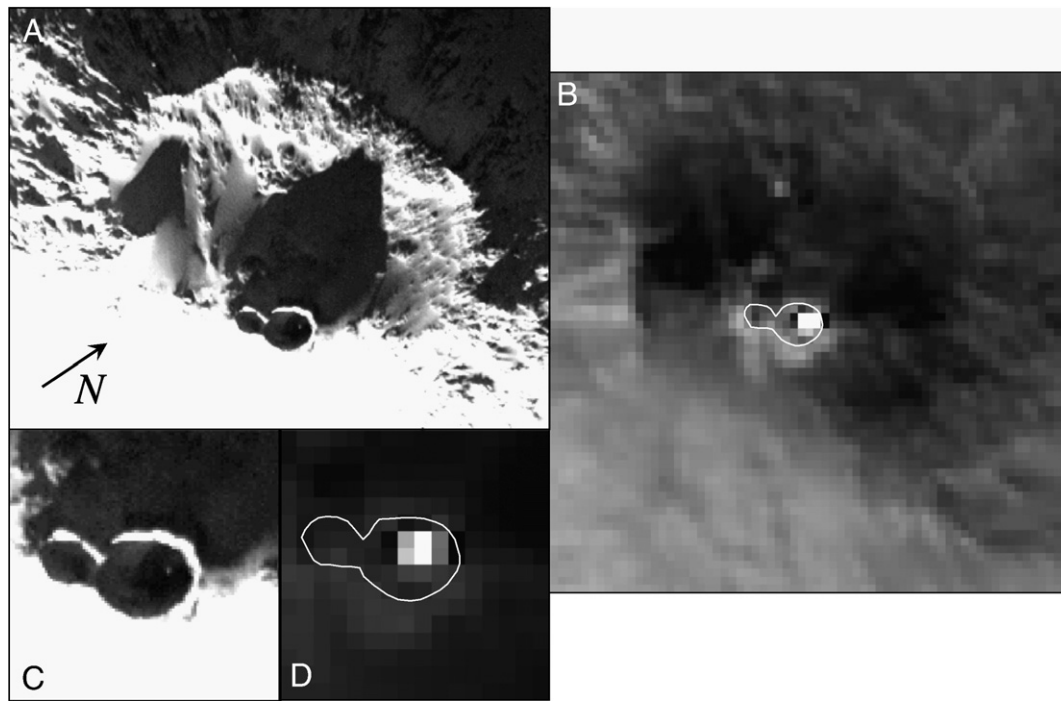
Fig. 10. ASTER images of Mount Erebus, acquired at 14:00:21 UT on 2005 December 13. This observation was nearly simultaneous with observations obtained on the ground with the ThermaCAM P65 infrared camera (image IR_0953). A. NIR channel 3 — the crater is about 500 m in diameter. B. TIR channel 13 — at the same scale as A (note craters outlined in white). C. Zoom image of channel 3 enhancing the thermally emissive pixels in the crater. D. Zoom of channel 13 image. Of the six brightest pixels, the two in the centre are the two hottest pixels that contain the lava lake (note craters outlined in white).

channel and defined as a background value that was subtracted from the radiance values of the lava lake pixels to correct for reflectance contribution to the signal.

In ASTER channel 2 (0.661 μm) there were no thermally emissive pixels in the Mount Erebus crater; therefore all radiance was due to solar reflection. Based on the minimum measurable emitted radiance for this channel, which corresponds to a brightness temperature of 1071.28 K (798.13 °C), this suggests a maximum temperature for the hottest portion of the lava lake at that time. This maximum temperature is consistent with that measured concurrently in the field with the thermal infrared cameras (mentioned previously). ASTER channel 3 (0.807 μm) measured four above-background radiant pixels coincident with the lava lake. The measured radiance values (adjusted for the background reflected component) and the calculated radiometric temperatures for these 4 pixels are shown in Table 6.

At 0.807 μm, thermal radiance is not measurable until target temperatures are above ≈900 K (≈626 °C). For the brightest of the 4 pixels, with a 15-m pixel-integrated brightness temperature of 1048.68 K (775.53 °C), it is possible, although unlikely, that the entire pixel contained material homogenously radiating at this temperature. More likely is that the pixel contained a mixture of cooler crusted lava in addition to the hot molten lava (two-component model). Previous studies have reported cooler crust temperatures ranging from 473 to

1061 K (100 to 788 °C) (Harris et al., 1999a), values consistent with those seen with the hand-held infrared cameras. Estimating crust temperatures using the VNIR data alone would be biased in favor of temperatures >900 K and would possibly over estimate sub-pixel temperatures. Longer wavelength measurements were used to calculate more realistic models of lava lake temperature components.

5.2.4. SWIR data analysis (30-m pixels)

The SWIR region is often used for measuring high-temperature (423–1473 K [150–1200 °C]) volcanic features because these wavelengths are most sensitive to thermally emitted radiance at these temperatures (Francis and Rothery, 1987; Rothery et al., 1988; Pieri

Table 5
ASTER TIR spectral emissivities

ASTER TIR Channel	Center wavelength (um)	Emissivity (1-reflectance) basanite	Emissivity (TεS) hot pixel #1	Emissivity (TεS) hot pixel #2
10	8.287	0.95616	0.879	1.000
11	8.635	0.93306	0.638	0.970
12	9.079	0.89676	0.625	0.890
13	10.659	0.88922	0.574	0.779
14	11.289	0.90822	0.543	0.719

Table 6
Surface radiance (W m^{-2} str^{-1} μm^{-1}) and pixel-integrated temperatures (PIT) for channel 3 (four hot pixels), channel 4 (saturated pixel), and all TIR channels (two hot pixels each). TεS-derived surface kinetic temperatures (Kin Temp) for the TIR pixels are also listed*

| ASTER channel	Hot pixel	Radiance (W/m²/um/sr)	PIT (°C)	PIT (K)
NIR ch 3	1	12.930	775.53	1048.68
NIR ch 3	2	9.482	756.74	1029.89
NIR ch 3	3	6.896	738.14	1011.29
NIR ch 3	4	5.172	721.90	995.05
SWIR ch 4	Saturated	55.220	452.22	725.37
TIR ch 10	1	23.791	87.35	360.50
TIR ch 10	2	23.688	87.03	360.18
TIR ch 11	1	17.309	66.66	339.81
TIR ch 11	2	17.303	66.64	339.79
TIR ch 12	1	16.745	67.71	340.86
TIR ch 12	2	15.763	63.37	336.52
TIR ch 13	1	13.749	60.73	333.88
TIR ch 13	2	12.536	53.40	326.55
TIR ch 14	1	12.216	53.82	326.97
TIR ch 14	2	10.905	44.74	317.89
Kin Temp*	1	—	93.65	366.80
Kin Temp*	2	—	64.25	337.40
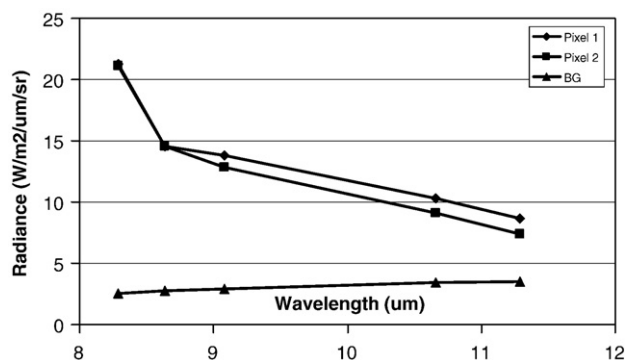
Fig. 11. ASTER TIR radiance values for the two hottest pixels that contain the lava lake, and the average background area (BG).

et al., 1990; Flynn et al., 1994; Oppenheimer and Francis, 1997; Harris et al., 1999a,b; Kaneko and Wooster, 2005). The amount of emitted radiance increases at all wavelengths with increasing temperature. Because of the Planck relationship between radiance and wavelength (peak radiance shifts to shorter wavelengths with increasing temperature), as temperatures approach 1000 K (727 °C) (as is the case for the Erebus lava lake) SWIR radiance increases more rapidly than radiance in the TIR region. This often results in saturated pixels in SWIR channels (Pieri et al., 1990; Oppenheimer and Francis, 1997; Wooster et al., 1997; Harris et al., 1999a). Saturation occurs when the radiance emitted from a pixel exceeds the upper sensitivity limit of the detector, which is controlled by the bit quantization level (8 bits pixel^{-1} for VIS–NIR and SWIR data; 12 bits pixel^{-1} for TIR data) and the radiometric gain coefficients. Any radiance in excess of this limit cannot be quantified (Wright et al., 1999).

All of the ASTER SWIR data analyzed in this study contain saturated pixels over the lava lake. While this prevents an absolute temperature determination, these data can at least be used to place a lower limit on the pixel-integrated temperatures measured for the 30-m pixels. Among the SWIR channels, ASTER channel 4 (1.657 um) has the largest range of possible radiometric temperatures that can be quantified: from 493.45 to 720.03 K (220.30 to 446.88 °C). Each of the four saturated pixels in channel 4 must contain sub-pixel temperature components whose fractional areas and temperatures combined exceed a pixel-integrated temperature of 725.37 K (452.22 °C), causing saturation (see Table 6). This minimum temperature is consistent with the field- measured temperatures and the VIS–NIR data analysis. The tendency for saturation in the SWIR channels emphasizes the importance of the TIR subsystem to identify the full range of temperature components, including molten lava, cooler lava crusts, and non- thermally radiant background surfaces.

5.2.5. TIR data analysis (90-m pixels)

There are no saturated pixels in the TIR radiance data analyzed in this study. This is primarily due to the larger pixel size. For 90-m TIR pixels, the lava lake is a sub-pixel feature, and even though the high temperatures derived from the VIS–NIR and SWIR data analyzes would saturate ASTER TIR data if they had the same pixel sizes, the large TIR pixels include cold, non-lava lake background surfaces and cause the pixel-integrated radiances and derived temperatures to be much lower (Table 6).

In the TIR data, there were two thermally-anomalous pixels with radiance spectra that indicate high temperatures (Fig. 11), so it was assumed that the radiance emitted from the lava lake was split between these two pixels. The surface kinetic temperatures calculated for each pixel were 366.8 K (93.65 °C) and 337.4 K (64.25 °C), respectively. These temperatures are slightly higher than the brightness temperatures derived from the radiance data for each TIR channel using the assumed emissivity of basanite (Table 6). This difference is due to the TεS

temperature retrieval method, which calculated lower (and presumably more accurate) emissivities for the surface (Gillespie et al., 1998).

Following the methods of prior studies that used multi-channel (either *Landsat* or ASTER) data, a two-temperature component model was used to estimate the size and average temperature of the lava lake within an ASTER TIR pixel (Rothery et al., 1988; Pieri et al., 1990; Harris et al., 1999b; Pieri and Abrams, 2005; Harris and Ripepe, 2007; Vaughan et al., 2007). In this case, the fractional area of the lava lake within the pixel (p_h) and the spectral radiance of the lava lake surface at temperature T ($L_{\lambda(T_h)}$) can be derived from Eq. (13) such that:

$$p_{\mathrm{h}} = \left[(R_\lambda/\varepsilon_\lambda) - L_{\lambda(T_{\mathrm{b}})} \right] / \left[L_{\lambda(T_{\mathrm{h}})} - L_{\lambda(T_{\mathrm{b}})} \right] \tag{14}$$

$$L_{\lambda(T_{\mathrm{h}})} = \left(\left[(R_\lambda/\varepsilon_\lambda) - L_{\lambda(T_{\mathrm{b}})} \right] / p_{\mathrm{h}} \right) + L_{\lambda(T_{\mathrm{b}})} \tag{15}$$

where T_{b} and T_{h} are the temperatures of the background and lava lake, respectively.

The only assumption is background temperature (T_{b}), which in this case was derived from the ASTER kinetic temperatures for areas in the crater that do not include the lava lake, which have an average temperature of 246 K (−27 °C). For each ASTER channel, a plot of p_{h} versus T_{h} for a range of realistic lava lake temperatures should show curves that intersect at a unique p_{h} versus T_{h} value. In practice, there are multiple intersections, but some of these can be eliminated as unrealistic while the meaningful one are clustered together. Fig. 12 shows the two-component pixel model and a plot of p_{h} versus T_{h} for ASTER TIR channels for the brightest pixel. With no a priori knowledge of the size or temperature of the lava lake, this model estimates that
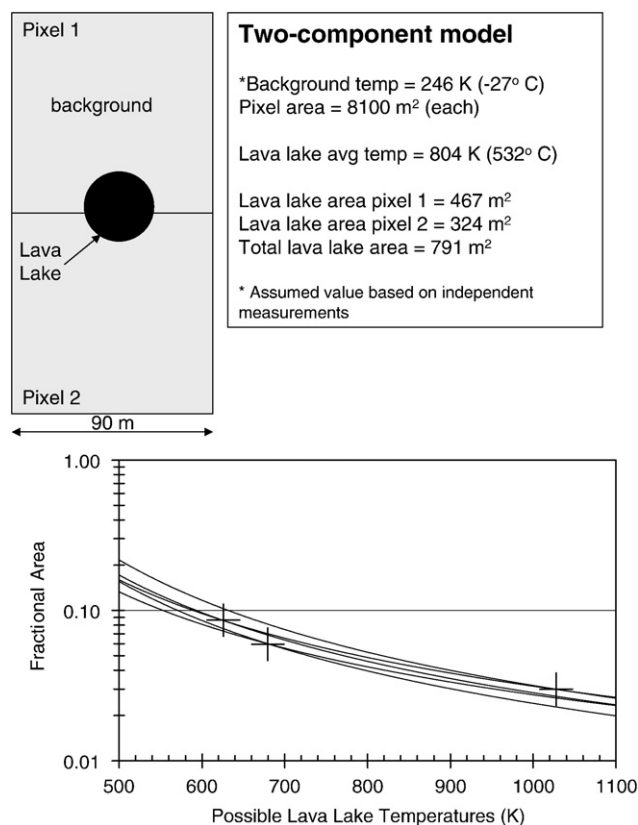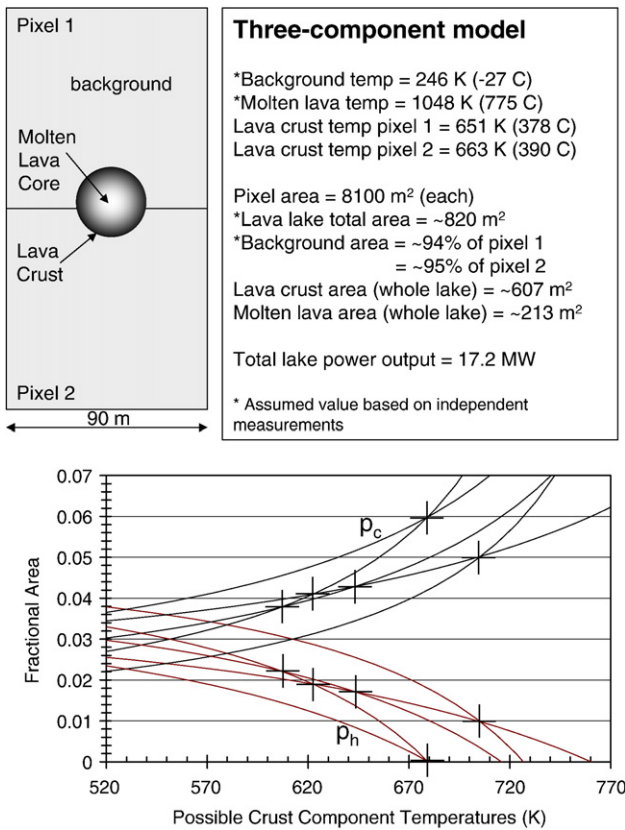

Fig. 12. Analysis of ASTER TIR data of the Erebus lava lake using a two-component pixel model, and a plot of p_{h} versus T_{h} for ASTER TIR channels for the brightest pixel. Crosses mark intersections at 0.03, 1026 K; 0.06, 679 K; and 0.083, 633 K. The average position of these intersections in p_{h}–T_{h} space is 0.058, which corresponds to an area of 467 m^2, at 780 K. The second pixel contains 324 m^2 of the lava lake at 829 K. This results in a model lake area of 791 m^2 with an average temperature of 804 K.

Fig. 13. Analysis of ASTER thermal infrared data of the Mount Erebus lava lake using a three-component model, and a plot of p_h and p_c versus T_c for ASTER TIR channels for the brightest TIR pixel. For the crust component (black lines), crosses mark intersections at 0.038, 606 K; 0.041, 623 K; 0.043, 643 K; 0.06, 680 K; and 0.05, 704 K. The average position of these intersections in p_c–T_c space corresponds to an area of 342 m^2 at 651 K in pixel 1, and a lake area of 264 m^2 at 663 K. The molten component (assumed to be 1048 K) occupies 100 m^2 in pixel 1 and 113 m^2 in pixel 2.

the average temperature of the lake is ∼804 K (532 °C) and the total area is ∼791 m^2.

It is more realistic, however, to assume that there is a heterogeneous thermal structure on the lava lake surface, which can be simplified into two components, a hot molten core and cooler crusted lava. In this case, there are a total of three thermal components to be modelled: the hot molten lava, cooler crusted lava, and the non-lava lake background. Harris et al. (1999b) developed a method for solving a three- component system, particularly for the case of a small lava lake within a pixel. For a three-component system, the pixel-integrated radiance emitted at wavelength λ ($R_λ$), corrected for atmospheric affects, can be written as

$$R_λ = ε_λ\big[p_h L_{λ(T_h)} + p_c L_{λ(T_c)} + p_b L_{λ(T_b)}\big] \qquad (16)$$

where p_b=portion of the pixel not occupied by thermally radiant lava lake (background); p_c=portion of the pixel occupied by crusted (cooled) lava; p_h=portion of the pixel occupied by hot molten lava=1− p_b−p_c; and T_b, T_c, and T_h, are the temperatures of the background, crust, and hot molten lava, respectively.

This approach required more assumptions as well as at least three concurrent spectral radiance measurements with the same spatial resolution (e.g., ASTER's five TIR channels). The temperature of the background (T_b) was assumed to be 246 K (−27 °C) based on averaging the surface kinetic temperature measurements of 20 pixels around, but not including, the thermal source. This temperature is consistent with background surface temperatures reported concurrently and in previous studies (Harris et al., 1999a). The temperature of the hot molten lava (T_h) was assumed to be 1048 K (775 °C) based on the

highest ASTER VNIR-derived temperature and concurrent ground-based temperature measurements. As before, the basanite emissivities were used for the background surface and cooler lava crusts. However, based on other research that shows how emissivity can vary as rocks approach molten temperatures (Abtahi et al., 2002), the emissivities used for the hot temperature component were derived from the ASTER surface emissivity data product for the hot pixels.

Based on the size of the lava lake, known from ground-based measurements to be ≈820 m^2, it is possible for it to be entirely contained within one 90-m pixel, in which case it would occupy ≈11% of the pixel area (p_c+p_h=0.1086; p_b=0.8914). So, with the lake split between 2 pixels, it occupied ≈6% and ≈5% of hot pixels 1 and 2, respectively.

These assumptions left only three unknowns: T_c, p_c, and p_h. Previous studies of Erebus have helped define a realistic range of possible crust temperatures (T_c) from as low as 473 K (100 °C) up to 1061 K (788 °C) (Harris et al., 1999a). From Eq. (16),

$$p_h = \big([R_λ/ε_λ] − p_b\big[L_{λ(T_b)}\big] − L_{λ(T_c)} + p_b\big[L_{λ(T_c)}\big]\big)/\big[L_{λ(T_h)} − L_{λ(T_c)}\big] \qquad (17)$$

and

$$p_c = \big([R_λ/ε_λ] − p_b\big[L_{λ(T_b)}\big] − L_{λ(T_h)} + p_b\big[L_{λ(T_h)}\big]\big)/\big[L_{λ(T_c)} − L_{λ(T_h)}\big]. \qquad (18)$$

These two values were calculated for the range of possible T_c values for each channel and plotted in p_h and p_c versus T_c space (Fig. 13). Theoretically, simultaneous spectral radiance measurements of the same pixel should generate curves that all intersect at a point corresponding to a unique T_c and fractional area (either p_c or p_h). In practice, there are multiple intersections observed and some curves that do not intersect at all within the zone of possible solutions.

Curves converge, on average, at T_c=≈651−663 K (≈378−390 °C); p_c=0.035–0.046; and p_h=0.014–0.015. This means that the thermal structure of the lava lake was characterized by ≈30% (213 m^2) molten lava and ≈70% (607 m^2) cooler crusted lava. Under these conditions the power output from the lake surface (Q_{rad}=σεT_h^4+σεT_c^4) was ≈17.2 MW (Fig. 13) and the radiant thermal flux was ≈109 kW m^{-2}.

5.3. MODIS

The MODIS instruments on *Terra* and *Aqua* have obtained over 4290 observations of Mount Erebus over a six-year period since 26 February 2000 (Wright and Pilger, 2008-this issue). Wight and Pilger found that the thermal emission from the lava lake, as determined from analysis of nighttime MODIS data, averaged ≈15 MW, with a standard deviation of ≈8 MW and a maximum value of ≈100 MW. This six-year average is consistent not only with previous analyses of remote sensing data (Glaze

Table 7
Comparison of analyses of different datasets of Erebus lava lake thermal emission

Instrument	Temperature range (K)	Area (m^2)	Radiative thermal emission, Q_{rad} (MW)	Notes
Hand-held thermal camera (ThermaCAM P65)	575–1090 807 (=T_{eff})	817–820	18.9[a]	Ground-truth
ASTER	T_c=651–663 T_h=1048	A_c=607 A_h=213 Total=820	17.2	TIR data
Hyperion	907–995	909	41.7	Daytime data: mostly saturated
MODIS	–	–	44	Daytime data: TIR data at km pixel^{-1} resolution

T_c, T_h, A_c, and A_h are the temperatures (T) and areas (A) of the crust and the hot molten components, respectively T_c, T_h, A_c, and A_h are the temperatures (T) and areas (A) of the crust and the hot molten components, respectively.
[a] Including convective heat loss, total lake heat loss is 23.5 MW.

et al., 1989; Harris et al., 1997, 1999a), but with estimates from the 2004 and 2005 thermal camera data.

The MODIS data obtained simultaneously with the ASTER observation on 2005 December 13 yielded a value for thermal emission of 44 MW. This over-estimated thermal output from the lava lake by the same factor as that derived from the Hyperion data because the MODIS instrument was also detecting thermal emission in the thermal infrared from the rest of the pixel (1 km^2), a factor that was corrected for in the analysis of the ASTER data. The lava lake occupies less than 0.1% of the area of a MODIS pixel in the thermal infrared.

6. Discussions

6.1. Instrument results comparison

Table 7 shows the results obtained from analysis of Hyperion, ASTER, and MODIS data. The Hyperion and MODIS data are less useful due to the presence of incident sunlight and, in the case of Hyperion, detector saturation. There is no real substitute for data obtained at night. Even though the amount of incident sunlight is very small at TIR wavelengths, it is still necessary to correct ASTER data and remove it. The instrument that most closely reproduces what is seen by the infrared camera on the ground is ASTER. ASTER's high spatial resolution, even in the thermal infrared, is sufficient to accurately determine colour temperatures and emitting areas, and therefore the integrated thermal emission spectrum. ASTER also demonstrates that thermal emission can be accurately constrained with relatively few bands (in this case, three), even when close together in the thermal infrared part of the electromagnetic spectrum.

6.2. Lava lakes on Io

What of lava lakes on Io? Good temporal coverage of volcanic activity at individual locations on Io, from ground-based instruments as well as from spacecraft (*Voyager*, *Galileo*, *Cassini* and, in early 2007, *New Horizons*), has allowed different styles of explosive and effusive activity at individual eruption styles to be identified. Examples include lava fountains and extensive flows at Pillan and Tvashtar, and the
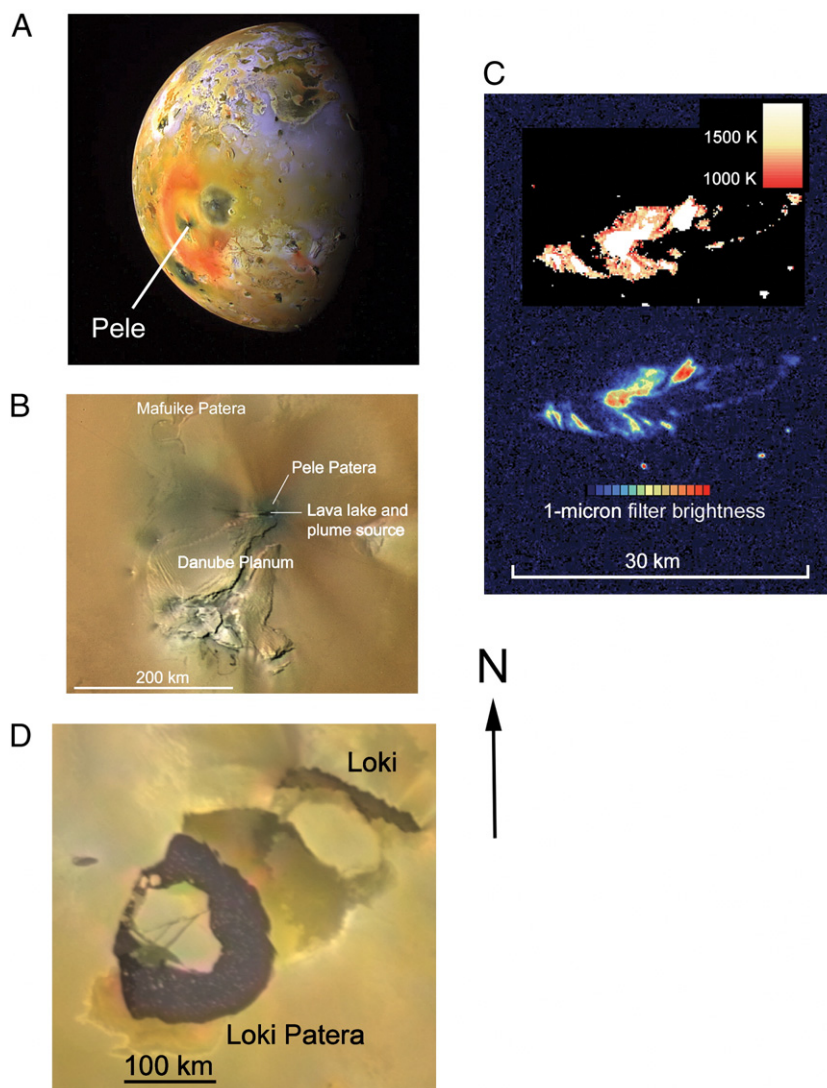
Fig. 14. Probable active lava lakes on Io. (A) Pele is located on the Jupiter-facing hemisphere of phase-locked Io at the centre of a red, sulphur-rich deposit over 1000 km across. (B) The Pele lava lake is located in a graben at the end of Danube Planum, abutting Pele Patera. (C) A high-resolution *Galileo* SSI nighttime image of Pele, showing the extent of activity and map of colour temperatures (Radebaugh et al., 2004). There is no high-resolution visible imagery of Pele in daylight. (D) Loki Patera: a feature some 200 km across, Loki Patera exhibits all the characteristics of a lava lake that quiescently overturns via crustal foundering (e.g., Rathbun et al., 2002; Davies, 2003b). The sheer size of this feature (the low-albedo patera floor has an area of 21,000 km^2) has led to Loki Patera being described as a magma sea, rather than a lava lake (Matson et al., 2006). There are no high-resolution images of Janus Patera, another possible lava lake (see Davies, 2007).

overturning lava lake at Pele (Davies et al., 2001, Milazzo et al., 2005); semi-periodic quiescent foundering at Loki Patera (Rathbun et al., 2002; Davies, 2003b; Matson et al., 2006), and pahoehoe-like flow field emplacement at Prometheus (Davies et al., 2006c).

Some volcanic activity on Io is limited to within, or in the immediate vicinity of, caldera-like depressions called *paterae* (for example, see Radebaugh et al., 2002), and the analysis of time-series thermal emission data allows constraint of possible eruption mechanisms. The observed thermal emission spectra and temporal evolution of thermal emission indicates that at least three of these features, Pele, Loki Patera, and Janus Patera, are active lava lakes (e.g., Davies et al., 2001; Rathbun et al., 2002; Davies, 2003b; Radebaugh et al., 2004; Davies, 2007). Fig. 14 shows images of Pele and Loki Patera.

Each of these hot spots exhibits thermal and temporal behaviour indicative of different styles of lava lake resurfacing (see Davies, 2007), reproducing the different stages of activity seen on Earth at basaltic lava lakes such as the Kupaianaha lava lake that formed on Kilauea in the 1980s (Flynn et al., 1993). Flynn et al. classified surface and thermal activity into three stages. Stage 1 activity was characterized by active lava fountains and rifting, resulting in the highest thermal emission from the lake. Stage 2 was marked by rifting events between plates of crust. Times of quiescence, when a thickening crust covered the surface of the lake, were designated as Stage 3. Over 99% of the time the Kupaiahana lava lake was quiescent (Stage 3) (Flynn et al., 1993).

Pele is unique on Io as having an infrared spectrum indicating that the crust on the lava lake is being continually disrupted, most likely by sulphurous volatiles degassing from the magma into the vacuum above Io's surface. These volatiles then entrain silicate material and form the diffuse, ephemeral Pele plume, which can exceed 300 km in height, and which lays down a red, annular deposit some 1200 to 1550 km in diameter.

Resurfacing at Loki Patera, a feature over 170 km in diameter, is consistent with the quiescent foundering of the crust on a lava lake (Rathbun et al., 2002; Davies, 2003b; Matson et al., 2006; Rathbun and Spencer, 2006). The active, emitting area of Loki Patera, over 21,000 km^2, has led to this feature's being described as a magma sea, rather than a lava lake (Matson et al., 2006).

Janus Patera exhibits a more episodic nature, more akin to what was observed at Kupaianaha, Hawai'i (Flynn et al., 1993). Janus is generally relatively quiescent, with an infrared thermal emission spectrum indicative of mostly cooling crust, but with the periods of elevated thermal emission that are expected from active overturning, when more incandescent lava is exposed.

The closest ionian analogue to the Erebus lava lake is most likely Pele. As seen by NIMS, the Pele lava lake almost always shows a preponderance of thermal emission at short wavelengths. This is indicative of vigorous exposure of incandescent and merely hot lava, without an increase in thermal emission at longer wavelengths expected from the emplacement and cooling of flows. The shapes of the thermal emission spectrum from Pele at six different times are shown in Fig. 3 of Davies et al. (2001). Fig. 15 shows the thermal spectra normalized to the peak thermal emission seen on each occasion (dividing the spectrum by the peak spectrum value). The peak of thermal emission from Pele varies between 2.5 and 5 μm, indicating that the effective emitting temperature is between 1160 K and 580 K. The hump in the G8 data at 1.8 μm indicates the presence of a very hot component, determined by Davies et al. (2001) to be at temperature of 1077 ± 13 K. This is the effective temperature of the hot component, made up of a range of different areas at different high temperatures (Davies et al., 2001). Thermal emission from Erebus peaks at a wavelength of 3.4 μm, indicating an effective temperature of 852 K (using Wein's law). This, of course, assumes an isothermal emitting source (which we know is not the case).

The scale of activity at Pele dwarfs that of Erebus (Davies, 2007). Area, radiative heat loss, and mass flux from these two volcanoes are compared in Table 1. Considering radiative thermal emission and associated effusion rate, for examples, Pele exceeds Erebus by four orders of magnitude. However, the shape of the thermal emission curve for actively overturning lava lakes does appear to scale invariantly, indicating that the temperature and area distributions are similar.

Thermal emission seen in most normalized Pele spectra at wavelengths shorter than 3 μm exceeds that seen from Erebus (see Fig. 16). The spectral regions of Pele's excess normalized thermal emission can be attributed to (1) hotter magma, perhaps up to 1600 K (Davies et al., 2001), (2) the disruption of the surface crust by escaping volatiles, exposing hot, molten lava beneath, and (3) small lava fountains contributing to short-wavelength thermal emission. Such relatively large high-temperature areas are not seen at Erebus except during Strombolian explosions.
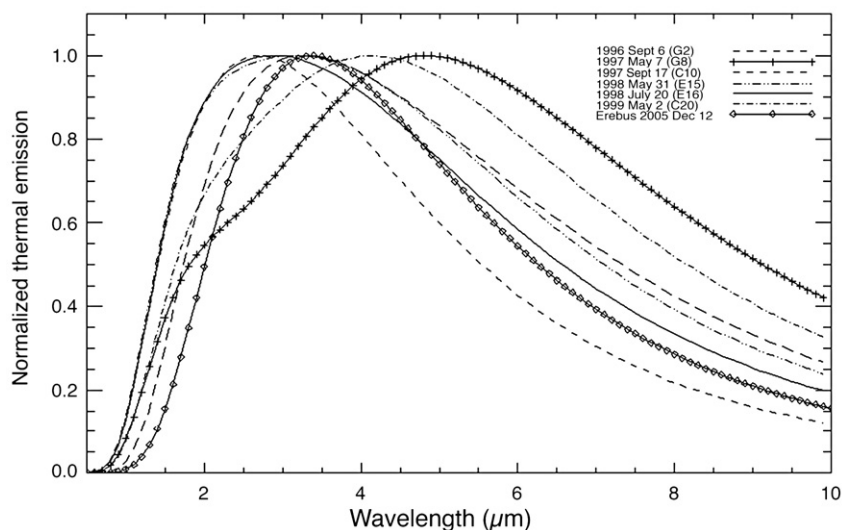
Fig. 15. Comparison of normalized, integrated thermal emission spectra of Pele, Io, and Ray Lake, Erebus, Antarctica. Each spectrum is divided by the peak thermal emission value on that day. The Pele data are from analyzes of *Galileo* NIMS data (Davies et al., 2001). The Ray Lake data are from infrared camera image IR_0936. Key: Pele. Small dashes = 6 September 1996 (*Galileo* orbit G2). Crosses = 7 May 1997 (Orbit G8). Large dashes = 17 September 1997 (Orbit C10). Dash-dot-dot-dot = 31 May 1998 (Orbit E15). Solid line = 20 July 1998 (Orbit E16). Dash-dot-dash-dot = 2 May 1999 (Orbit C20). Diamonds = Erebus, IR_0936, 13 December 2005.
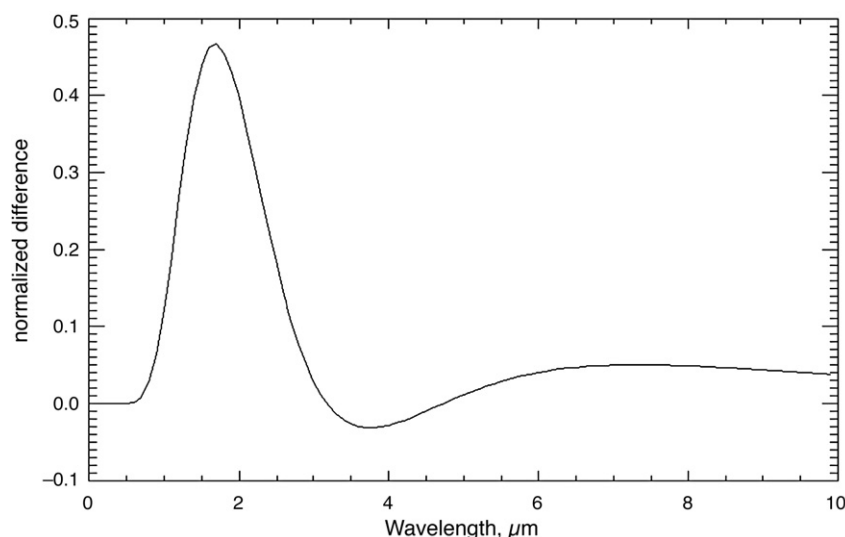
Fig. 16. Subtraction of normalized Erebus lava lake (Ray Lake) thermal emission spectrum from normalized Pele (Orbit E16) lava lake data, to illustrate where Pele proportionally emits more energy (where the normalized difference is positive). Between 0.5 μm and 3.2 μm, normalized Pele emits more energy than Ray Lake, possibly due to some or all of the following: (1) crust disruption by exsolving gas; (2) hotter magma exposed; (3) lava fountaining exposing incandescent lava. Between 3.2 μm and 4.25 μm, normalized Ray Lake emits proportionally more than Pele, an indication of the relatively narrow range of high temperatures present at Ray Lake. At longer wavelengths longer Pele emits proportionally slightly more energy than Erebus. This is due to large, relatively cool areas forming some distance away from the portion of the lake being disrupted by the Pele plume, areas at temperatures that are not present at Ray Lake.

Scale aside, there are many similarities between Erebus and Pele. Both are long-lived-active lava lakes (Pele has been seen in every appropriate observation since 1979), with circulating magma. The two lava lakes have a restricted range of surface temperatures, the result of surface crust recycling. The similarities between the temporal behaviour of thermal emission and the shape of the thermal spectra at Erebus and Pele are further evidence that Pele is a lava lake.

7. Conclusions

In 2005 Erebus was erupting in a manner similar to previous years (see Wright and Pilger, 2008-this issue). Total heat loss from the lava lake was ≈23.5 MW. The main change from 2004 (see Calkins et al., 2008-this issue) was that there was only one lava lake present in 2005.

A new technique is demonstrated for separating sunlight from thermal emission data, using a simple probabilistic model (Supplemental Material). This methodology is currently being incorporated into the JPL Volcano Sensor Web in order to fully automate the quantification of thermal emission and the generation of effusion rate estimates. The Sensor Web optimises spacecraft resource use, and is proving invaluable for obtaining many observations of active volcanoes around the world. Spacecraft data (Hyperion, ALI, MODIS) obtained contemporaneously with the ground-based thermal camera data were somewhat compromised by incident sunlight.

The least-affected data were obtained by ASTER, where a combination of data at thermal infrared wavelengths and relatively high spatial resolution yielded the most accurate determinations of temperature and emitting area. This work demonstrates (once again) that there is no substitute for nighttime data for accurately quantifying thermal emission data at visible and SWIR wavelengths. What is needed, therefore, are FLIR ThermaCAM or equivalent nighttime data of the lava lake. Although instruments and power supplies do not generally survive deep into the Antarctic winter, it may be possible to develop a cheap, expendable camera (a FLIR ThermaCAM P65 costs more than $50,000). Such an asset could obtain data in the early autumn during short nights. Data could again be collected in conjunction with nighttime spacecraft observations. This would enable visible and SWIR data from Hyperion, ALI and ASTER to be tested against this ground-truth without errors introduced by the need to remove sunlight.

The integrated thermal emission spectrum from the Erebus lava lake bears a striking similarity to that obtained by the *Galileo* spacecraft for the ionian volcano Pele, also thought to be an active, overturning lava lake, albeit one on a much larger scale.

This similarity suggests that similar styles of magma eruption are taking place at these two locations on two different planetary bodies. This insight might lead to a greater understanding of magma supply mechanism to Pele through a more detailed comparison with Erebus. The short wavelength thermal emission from Pele is proportionally larger than that seen at Erebus because of hotter magma at Pele and a greater disruption of the surface gas as volatiles escape from the lava lake into a vacuum. There are times, however, when Erebus would exhibit similar or greater short-wavelength normalized thermal emission than Pele. This state occurs during Strombolian eruptions of Erebus, but these only occur considerably less than 1% of the time.

Finally, the field deployment to Antarctica in December 2005 was successful in obtaining high-quality, calibrated data of the temperature and area distribution of the Erebus lava lake (Ray Lake), which allowed the integrated thermal emission spectrum of the lava lake to be derived for the first time. This spectrum was the main goal of this work: to establish ground-truth in order to provide test input to models of volcanic thermal emission. In particular, these data will be used to test the Davies (1996) thermal emission model, which has been used to model telescope and spacecraft multispectral and hyperspectral data of volcanism on Io. The results and analysis from that model testing are described elsewhere (Davies et al., 2008).

Appendix A. Supplementary data

Supplementary data associated with this article can be found, in the online version, at doi:10.1016/j.jvolgeores.2008.02.010.

References

Abtahi, A.A., Kahle, A.B., Abbot, E.A., Gillespie, A.R., Sabol, D., Yamada, G., Pieri, D.C., 2002. Emissivity changes in basalt cooling after eruption from Pu'u O'o [abstract]: Eos (Transactions, American Geophysical Union), vol. 83. V71A-1263.

Aster, R., McIntosh, W., Kyle, P., et al., 2004. Real-time data received from Mount Erebus Volcano, Antarctica. EOS Transactions 85, 97–101.

Belton, M.J.S., Klaasen, K.P., Clary, M.C., et al., 1992. The *Galileo* solid-state imaging experiment. Space Science Reviews 60, 413–455.

Blaney, D.L., Johnson, T.V., Matson, D.L., et al., 1995. Volcanic eruptions on Io: heat flow, resurfacing, and lava composition. Icarus 113, 220–225.

Calkins, J., Oppenheimer, C., Kyle, P.R., 2008. Ground-based thermal imaging of phonolite lava lakes at Erebus volcano, Antarctica in December 2004. J. Volcanol. Geotherm. Res. 177, 695–704 (this issue). doi:10.1016/j.jvolgeores.2008.02.002.

Carlson, R.W., Weissman, P.R., Smythe, W.D., et al., 1992. Near-infrared mapping spectrometer experiment on *Galileo*. Space Science Reviews 60, 457–502.

Carr, M.H., 1986. Silicate volcanism on Io. Journal of Geophysical Research 91, 3521–3532.

Chien, S., Sherwood, R., Tran, D., et al., 2005. Using autonomy flight software to improve science return on Earth observing one. Journal of Aerospace Computing, Information & Communication 2, 196–216 AIAA.

Davies, A.G., 1996. Io's volcanism: thermo-physical models of silicate lava compared with observations of thermal emission. Icarus 124, 45–61.

Davies, A.G., 2003a. Volcanism on Io: estimation of eruption parameters from Galileo NIMS data. Journal of Geophysical Research (Planets) 108, 5106–5120.

Davies, A.G., 2003b. Temperature, age and crust thickness distributions of Loki Patera on Io from Galileo NIMS data: implications for resurfacing mechanism. Geophysical Research Letters 30, 2133–2136.

Davies, A.G., 2007. Volcanism on Io: a comparison with Earth. Cambridge University Press, Cambridge. 376 pages.

Davies, A.G., Keszthelyi, L.P., 2005. Classification of volcanic eruptions on Io and Earth using low-resolution remote sensing data. Lunar and Planetary Sciences Conference XXXVI. Abstract #1963.

Davies, A.G., McEwen, A.S., Lopes-Gautier, R., et al., 1997. Temperature and area constraints of the South Volund Volcano on Io from the NIMS and SSI instruments during the *Galileo* G1 orbit. Geophysical Research Letters 24, 2447–2450.

Davies, A.G., Keszthelyi, L.P., Williams, D.A., et al., 2001. Thermal signature, eruption style, and eruption evolution at Pele and Pillan on Io. Journal of Geophysical Research 106, 33079–33104.

Davies, A.G., Matson, D.L., Veeder, G.J., et al., 2005. Post-solidification cooling and the age of Io's lava flows. Icarus 176, 123–137.

Davies, A.G., Chien, S., Baker, V., et al., 2006a. Monitoring active volcanism with the autonomous sciencecraft experiment on *EO-1*. Remote Sensing of Environment 101, 427–446.

Davies, A.G., Chien, S., Wright, R., et al., 2006b. Sensor web enables rapid response to volcanic activity. EOS 87 1&5.

Davies, A.G., Wilson, L., Matson, D.L., et al., 2006c. The heartbeat of the volcano: the discovery of episodic activity at Prometheus on Io. Icarus 184, 460–477.

Davies, A.G., Keszthelyi L.P., Matson, D.L., Johnson, T.V., Veeder, G.J., Blaney, D.L., 2008. Validation of volcanic thermal emission models using ground-truthed data of the Erebus volcano (Antarctica) lava lake: implications for Io. Lunar Plan. Sci. Conf. XXXIX, abstract 1896 (on CD-ROM).

Doggett, T., Greeley, R., Chien, S., et al., 2006. Autonomous detection of cryospheric change with Hyperion on-board *Earth Observing-1*. Remote Sensing of Environment 101, 447–462.

Dozier, J., 1981. A method for satellite identification of surface temperature fields of subpixel resolution. Remote Sensing of Environment 11, 221–229.

Flynn, L.P., Mouginis-Mark, P.J., Gradie, J.C., et al., 1993. Radiative temperature measurements at Kupaianaha lava lake, Kilauea volcano, Hawai'i. Journal of Geophysical Research 98, 6461–6476.

Flynn, L.P., Mouginis-Mark, P.J., Horton, K.A., 1994. Distribution of thermal areas on active lava flow field: Landsat observations of Kilauea, Hawaii, July 1991. Bulletin of Volcanology 56, 284–296.

Francis, P.W., Rothery, D.A., 1987. Using Landsat thematic mapper data to detect and monitor active volcanoes: an example from Lascar Volcano, Northern Chile. Geology 15, 614–617.

Giggenbach, W.F., Kyle, P.R., Lyon, G.L., 1973. Present volcanic activity on Mount Erebus, Ross Island, Antarctica. Geology 1, 135–136.

Gillespie, A.R., Rokugawa, S., Matsunaga, T., Cothern, J.S., Hook, S.J., Kahle, A.B., 1998. A temperature and emissivity separation algorithm for advanced spaceborne thermal emission and reflection radiometer (ASTER) images. IEEE Trans. Geosci. Remote Sens. 36, 1113–1126.

Glaze, L.S., Francis, P.W., Rothery, D.A., 1989. Measuring thermal budgets of active volcanoes by satellite remote sensing. Nature 338, 144–146.

Greeley, R., Iverson, J., 1987. Wind as a Geological Process on Earth, Mars, Venus and Titan, 2nd ed. Cambridge University Press, Cambridge, UK.

Harris, A.J.L., Ripepe, M., 2007. Temperature and dynamics of degassing at Stromboli. Journal of Geophysical Research 112, B03205. doi:10.1029/2006JB004393.

Harris, A.J.L., Butterworth, A.L., Carlton, R.W., Downey, I., Miller, P., Navarro, P., Rothery, D.A., 1997. Low-cost volcano surveillance from space: case studies from Etna, Krafla, Cerro Negra, Fogo, Lascar and Erebus. Bulletin of Volcanology 59, 49–64.

Harris, A.J.L., Wright, R., Flynn, L.P., 1999a. Remote sensing of Mount Erebus Volcano, Antarctica, using polar orbiters: progress and prospects. International Journal of Remote Sensing 20, 3051–3071.

Harris, A.J.L., Flynn, L.P., Rothery, D.A., Oppenheimer, C., Sherman, S.B., et al., 1999b. Mass flux measurements at lava lakes: implications for magma recycling. Journal of Geophysical Research 104, 7117–7136.

Head, J.W., Wilson, L., 1986. Volcanic processes and landforms on Venus − theory, predictions, and observations. Journal of Geophysical Research 91, 9407–9446.

Howell, R.R., 1997. Thermal emission from lava flows on Io. Icarus 127, 394–407.

Howell, R.R., 2006. Corrigendum to "Thermal emission from lava flows on Io, Icarus, 127, 394–407". Icarus 182, 299.

Ip, F., Dohm, J.M., Baker, V.R., et al., 2006. Flood detection and monitoring with the autonomous sciencecraft experiment onboard *EO-1*. Remote Sensing Of Environment 101, 463–481.

Johnson, T.V., Veeder, G.J., Matson, D.L., et al., 1988. Io − evidence for silicate volcanism in 1986. Science 242, 1280–1283.

Johnson, J., Aster, R., Jones, K., Kyle, P.R., McIntosh, W.C., Gerst, A., 2008. Acoustic Source Characterization of Erebus Lava Lake Explosions. J. Volcanol. Geotherm. Res. 177, 673–686 (this issue).

Jones, K.R., Johnson, J.B., Aster, R.C., Kyle, P.R., McIntosh, W.C., 2008. Infrasonic tracking of large bubble bursts and ash venting at Erebus volcano, Antarctica. J. Volcanol. Geotherm. Res. 177, 661–672 (this issue). doi:10.1016/j.jvolgeores.2008.02.003.

Kaneko, T., Wooster, M.J., 2005. Satellite thermal analysis of the 1986 Izu-Oshima lava flows. Journal of Volcanology and Geothermal Research 148 (3-4), 355–371.

Keszthelyi, L., Denlinger, R., 1996. The initial cooling of pahoehoe flow lobes. Bulletin of Volcanology 58, 5–18.

Keszthelyi, L., McEwen, A.S., Phillips, C.B., et al., 2001. Imaging of volcanic activity on Jupiter's moon Io by *Galileo* during the *Galileo* Europa Mission and the *Galileo* Millennium Mission. Journal of Geophysical Research 106, 33025–33052.

Keszthelyi, L., Jaeger, W.L., Turtle, E.P., et al., 2004. A post-*Galileo* view of Io's interior. Icarus 169, 271–286.

Keszthelyi, L.P., Jaeger, W.L., Milazzo, M.P., Radebaugh, J., Davies, A.G. and Mitchell, K.L., 2007. New estimates for Io eruption temperatures: implications for the interior. Icarus, 192, 491–502.

Kyle, P.R., 1994. Volcanological and Environmental Studies of Mount Erebus. . Antarctic Research Series, vol. 66. American Geophysical Union. 162 pp.

Kyle, P.R., Dibble, R.R., Giggenbach, W.F., Keyes, J., 1982. Volcanic activity associated with the anorthoclase phonolite lava lake, Mt. Erebus, Antarctica. In: Craddock, C. (Ed.), Antarctic Geosciences. University of Wisconsin Press, pp. 735–745.

Matson, D.L., Davies, A.G., Veeder, G.J., et al., 2006. Io: Loki Patera as a magma sea. Journal of Geophysical Research (Planets) 111. doi:10.1029/2006JE002703.

McAdams, W.H., 1954. Heat Transmission. McGraw-Hill, New York.

McEwen, A.S., Simonelli, D.P., Senske, D.R., et al., 1997. High-temperature hot spots on Io as seen by the Galileo solid state imaging (SSI) experiment. Geophysical Research Letters 24, 2443–2446.

McEwen, A.S., Keszthelyi, L., Geissler, P., et al., 1998a. Active volcanism on Io as seen by *Galileo* SSI. Icarus 135, 181–219.

McEwen, A.S., Keszthelyi, L., Spencer, J.R., et al., 1998b. High-temperature silicate volcanism on Jupiter's Moon Io. Science 281, 87–90.

Milazzo, M.P., Keszthelyi, L.P, Radebaugh, J., et al., 2005. Volcanic activity at Tvashtar Catena, Io. Icarus 179, 235–251.

Morabito, L.A., Synnott, S.P., Kupferman, P.N., et al., 1979. Discovery of currently active extraterrestrial volcanism. Science 204, 972.

Oppenheimer, C., Francis, P., 1997. Remote sensing of heat, lava and fumarole emissions from Erta 'Ale volcano, Ethiopia. International Journal of Remote Sensing 18 (8), 1661–1692.

Pearlman, J.S., Barry, P.S., Segal, C.C., et al., 2003. Hyperion, a space-based imaging spectrometer. IEEE Transactions on Geoscience and Remote Sensing 41, 1160–1172.

Pieri, D.C., Abrams, M.J., 2005. ASTER observations of thermal anomalies preceding the April 2003 Eruption of Chikurachki Volcano, Kurile Islands, Russia. Remote Sensing of Environment 99, 84–94.

Pieri, D.C., Glaze, L.S., Abrams, M.J., 1990. Thermal radiance observations of an active lava flow during the 1984 eruption of Mount Etna. Geology 18, 1023–1027.

Radebaugh, J., McEwen, A.S., Milazzo, M., et al., 2002. Lava Lakes in Io's Paterae. AGU Spring Meeting Abstracts 21, 06.

Radebaugh, J., McEwen, A.S., Milazzo, M.P., et al., 2004. Observations and temperatures of Io's Pele Patera from Cassini and Galileo spacecraft images. Icarus 169, 65–79.

Rathbun, J., Spencer, J.R., 2006. Loki, Io: New ground-based observations and a model describing the change from periodic overturn. Geophysical Research Letters 33. doi:10.1029/2002GL014747.

Rathbun, J.A., Spencer, J.R., Davies, A.G., Howell, R., Wilson, L., 2002. Loki, Io: a periodic volcano. Geophysical Research Letters 29, 84–81.

Rothery, D.A., Francis, P.W., Wood, C.A., 1988. Volcano monitoring using short wavelength infrared data from satellites. Journal of Geophysical Research 93 (B7), 7993–8008.

Salomonson, V., Barnes, W., Maymon, P., Montgomery, H., Ostrow, H., 1989. MODIS: Advanced facility instrument for studies of the Earth as a system. IEEE Transactions on Geoscience and Remote Sensing 27 (4), 145–153.

Stansberry, J.A., Spencer, J.R., Howell, R.R., et al., 1997. Violent silicate volcanism on Io in 1996. Geophysical Research Letters 24, 2455–2458.

Thome, K., Palluconi, F., Takashima, T., Masuda, K., 1998. Atmospheric Correction of ASTER. IEEE Transactions on Geoscience and Remote Sensing 36 (4), 1199–1211.

Tonooka, H., Iwasaki, A., 2003. Improvement of ASTER/SWIR crosstalk correction. Proceedings of SPIE 5234, 168–179.

Ungar, S.G., Pearlman, J.S., Mendenhall, J.A., et al., 2003. Overview of the *Earth Observing One* (*EO-1*) Mission. IEEE Transactions in Geoscience and Remote Sensing 41, 1149–1159.

Vaughan, R.G., Abrams, M.J., Hook, S.J., Pieri, D.C., 2007. Satellite observations of new volcanic island and pumice rafts: Home Reef Seamount, Tonga. EOS 88 (4) 37 & 41.

Veeder, G.J., Matson, D.L., Johnson, T.V., et al., 1994. Io's heat flow from infrared radiometry: 1983–1993. Journal of Geophysical Research 99, 17095–17162.

Wardell, L.J., Kyle, P.R., Campbell, A.R., 2003. CO_2 emissions from fumarolic ice towers, Mt. Erebus volcano, Antarctica. In: Oppenheimer, C., Pyle, D.M., Barclay, J. (Eds.), Volcanic Degassing, vol. 213. Geological Society, London, pp. 231–246.

Wardell, L.J., Kyle, P.R., Chaffin, P.R., 2004. Carbon dioxide and carbon monoxide emission rates from an alkaline intra-plate volcano: Mount Erebus, Antarctica. Journal of Volcanology and Geothermal Research 131, 109–121.

Wooster, M.J., Wright, R., Blake, S., Rothery, D.A., 1997. Cooling mechanisms and an approximate thermal budget for the 1991–1993 Mount Etna lava flow. Geophysical Research Letters 24 (24), 3277–3280.

Wright, R., Flynn, L.P., 2003. On the retrieval of lava flow surface temperatures from infrared satellite data. Geology 31, 893–896.

Wright, R., Pilger, E., 2008. Satellite observations reveal little inter-annual variability in the radient flux from the Mount Erebus lava lake. J. Volcanol. Geotherm. Res. 177, 687–694 (this issue). doi:10.1016/j.jvolgeores.2008.03.005.

Wright, R., Rothery, D.A., Blake, S., Harris, A.J.L., Pieri, D.C., 1999. Simulating the response of the EOS Terra ASTER sensor to high-temperature volcanic targets. Geophysical Research Letters 26 (12), 1773–1776.

Yamaguchi, Y., Kahle, A.B., Tsu, H., Kawakami, T., Pniel, M., 1998. Overview of advanced spaceborne thermal emission and reflection radiometer (ASTER). IEEE Transactions on Geoscience and Remote Sensing 36 (4), 1062–1071.

Zreda-Gostynska, G., Kyle, P.R., Finnegan, D., Prestbo, K.M., 1997. Volcanic gas emissions from Mount Erebus and their environmental impact on the Antarctic environment. Journal of Geophysical Research 102 (B7), 15039–15055.